HUBBLE SPACE TELESCOPE STIS ULTRAVIOLET SPECTRAL EVIDENCE OF OUTFLOW IN EXTREME NARROW-LINE SEYFERT 1 GALAXIES. II. MODELING AND INTERPRETATION[1,2]

KAREN M. LEIGHLY

Department of Physics and Astronomy, The University of Oklahoma, 440 West Brooks Street, Norman, OK 73019; leighly@nhn.ou.edu

ABSTRACT

We present modeling to explore the conditions of the broad-line–emitting gas in two extreme narrow-line Seyfert 1 galaxies, using the observational results described in the first paper of this series. Photoionization modeling using CLOUDY was conducted for the broad blueshifted wind lines and the narrow, symmetric, rest-wavelength–centered disk lines separately. A broad range of physical conditions was explored for the wind component, and a figure of merit was used to quantitatively evaluate the simulation results. Of the three minima in the figure-of-merit parameter space, we favor the solution characterized by an X-ray–weak continuum, elevated abundances, a small column density ($\log N_{\rm H} \approx 21.4$), a relatively high ionization parameter ($\log U \approx -1.2$ to -0.2), a wide range of densities ($\log n \approx 7-11$), and a covering fraction of ~ 0.15. The presence of low-ionization emission lines implies that the disk component is optically thick to the continuum, and the Si III]/C III] ratio implies a density of 10^{10}–$10^{10.25}$ cm^{-3}. A low ionization parameter ($\log U = -3$) is inferred for the intermediate-ionization lines, unless the continuum is "filtered" through the wind before illuminating the intermediate-line–emitting gas, in which case $\log U = -2.1$. The location of the emission regions was inferred from the photoionization modeling and a simple "toy" dynamical model. A large black hole mass ($1.3 \times 10^8 \, M_\odot$) radiating at 11% of the Eddington luminosity is consistent with the kinematics of both the disk and wind lines, and an emission radius of $\sim 10^4 \, R_{\rm S}$ is inferred for both. We compare these results with previous work and discuss implications.

Subject headings: galaxies: Seyfert — quasars: emission lines — quasars: individual (IRAS 13224−3809, 1H 0707−495) — ultraviolet: galaxies

1. INTRODUCTION

In 1992, it was demonstrated by Boroson & Green that the optical emission line properties in the region of the spectrum around Hβ are strongly correlated with one another. A principal-component analysis allowed the largest differences among optical emission line properties to be gathered together in a construct commonly known as "Eigenvector 1." The strongest differences hinged on the strength of the Fe II and [O III] emission and on the width and asymmetry of Hβ. This strong set of correlations is remarkable, as it involves correlations among the dynamics and gas properties between regions separated by vast distances. Furthermore, the same set of correlations is observed in samples selected in many different ways. This pervasiveness leads us to believe that we are observing the manifestation of a primary physical parameter. The most favored explanation is that it is the accretion rate relative to the black hole mass onto the active nucleus.

Narrow-line Seyfert 1 galaxies (NLS1's) are identified by their optical emission line properties. They typically have narrow permitted optical lines (FWHM of Hβ < 2000 km s^{-1}) and weak forbidden lines ([O III]/Hβ < 3; this distinguishes them from Seyfert 2 galaxies), and they frequently show strong Fe II emission (Osterbrock & Pogge 1985; Goodrich 1989). These are the same properties that define the Boroson & Green (1992) Eigenvector 1, and indeed NLS1's fall at one end of Eigenvector 1. Thus, the study of NLS1's offers an attractive research opportunity: if we can understand the origin of the emission-line properties of NLS1's, then we may be in a position to understand active galactic nucleus (AGN) emission in general. Furthermore, because at least some of the lines in NLS1's are narrow, identification of the frequently strongly blended lines is less ambiguous than it is in broad-line objects.

This paper is the second in a series of two that explores the UV emission line properties of NLS1's. In the first paper (Leighly & Moore 2004, hereafter Paper I) we introduce the topic by discussing previous work on the UV emission line properties of NLS1's. We then present a detailed analysis of the *Hubble Space Telescope* Space Telescope Imaging Spectrograph (*HST* STIS) spectra of two NLS1's, IRAS 13224−3809 and 1H 0707−495, that are known for their extreme X-ray properties. We found that their continua are as blue as that of the average quasar. We observed that the high-ionization emission lines (including N V and C IV) are broad (FWHM ≈ 5000 km s^{-1}) and strongly blueshifted, peaking at around 2500 km s^{-1} and extending to almost ∼10,000 km s^{-1}. In contrast, the intermediate- and low-ionization lines (e.g., C III] and Mg II) are narrow (FWHM 1000–1900 km s^{-1}) and centered at the rest wavelength. Si III] is prominent, and other low-ionization lines (e.g., Fe II and Si II) are strong. On the basis of these observations, the working model that we adopted considers that the blueshifted high-ionization lines

come from a wind that is moving toward us, with the receding side blocked by the optically thick accretion disk, and that the intermediate- and low-ionization lines are emitted in the accretion disk atmosphere or low-velocity base of the wind.[3]

The strongly blueshifted C IV profile suggested that it is dominated by emission in the wind. Following Baldwin et al. (1996), we used the C IV profile to develop a template for the wind. We then used this template, plus a narrow and symmetric component representing the disk emission, to model the other bright emission lines. We inferred that the high-ionization lines N V and He II are also dominated by wind emission and that part of Lyα is emitted in the wind. A part of Lyα and the intermediate- and low-ionization lines Al III, Si III], C III], and Mg II are dominated by disk emission. The 1400 Å feature, composed of O IV] and Si IV, was difficult to model; however, it appears to include both disk and wind emission.

IRAS 13224−3809 and 1H 0707−495 have distinctive X-ray properties among NLS1's; to determine whether their distinctive properties carry over to the UV, we analyzed *HST* archival spectra from 14 other NLS1's with a range of 2 orders of magnitude in UV luminosity. We find indeed that these two objects are extreme in this sample with respect to the following properties: the strongly blueshifted C IV line; the low equivalent widths of many of the lines, particularly C IV and He II; high C III]/C IV, Si III]/C III], Al III/C III], and N V/C IV ratios; steep α_{ox}; and blue UV continuum. Correlation analysis finds a number of strong correlations. An anticorrelation between C IV asymmetry and equivalent width suggests that the line is generally composed of a highly asymmetric wind component and a narrower symmetric component. The anticorrelation between C IV asymmetry and α_{ox} and α_u, and with He II suggests that UV-strong and X-ray−weak continua may be associated with the wind, as would be expected if the acceleration mechanism is radiation line driving. The dominance of Al III and Si III] over C III] suggests that possibly the continuum is transmitted through the wind before it illuminates the intermediate- and low-ionization line-emitting gas.

In this paper, our goal is to use modeling to explore the physical conditions of the line emission gas. In § 2, we compute the predicted equivalent widths and ratios of the bright UV emission lines using the photoionization code CLOUDY (Ferland 2001) and then compare those with the observed values from IRAS 13224−3809 to constrain the ionization parameter, density, covering fraction, column density, and shape of the photoionizing continuum. In § 3, we assume a black hole mass and use the photoionization results to estimate the distance from the central engine to the line-emitting region. We obtain the distance directly for the disk emission but need to construct a toy dynamical model to obtain the distance for the wind. In § 4, we compare with previous results, discuss broader implications, and present a speculative scenario to tie all the results together.

2. PHOTOIONIZATION ANALYSIS

In Paper I, we showed that the broad-line region lines in the spectra from IRAS 13224−3809 and 1H 0707−495 can be fairly robustly separated into a broad blueshifted high-

ionization component and a narrow symmetric intermediate- and low-ionization component. Thus, these spectra present us with a rare opportunity to model these components separately and obtain physical constraints for the line-emitting gas in the two different emission regions.

We use the photoionization code CLOUDY, version 94.00 (Ferland 2001), to simulate the emission lines. Our approach is to simulate the line emission in the gas with a range of densities, column densities, and metallicities subject to a range of photoionizing fluxes, assuming several different continuum shapes. We then compare the predicted line equivalent widths and ratios with the observed values. Our approach is similar to that described by Baldwin et al. (1996), although it differs somewhat in the details of the method used for comparing the observed and predicted line properties, as described below.

2.1. *Continuum*

The lines emitted by AGNs should depend on the shape of the continuum (Krolik & Kallman 1988; Casebeer & Leighly 2004). Therefore, the first step in the photoionization modeling is to construct the continuum. Our two objects are essentially identical; therefore, since more multiwavelength information is available for IRAS 13224−3809 than for 1H 0707−495, we concentrate on developing a continuum for IRAS 13224−3809 and modeling it in detail.

There was no X-ray observation coordinated with the *HST* observation, so there is uncertainty in extrapolation of the *HST* spectra to the nonsimultaneous *ROSAT* and *ASCA* data. However, both IRAS 13224−3809 and 1H 0707−495 show high-amplitude X-ray variability on timescales of a few thousand seconds (e.g., Leighly 1999a; Boller et al. 1997), and defining an average X-ray continuum would be ambiguous even if simultaneous observations were available. For IRAS 13324−3809, we used the average *ASCA* spectrum from the observation conducted on 1994 July 30 and the average *ROSAT* PSPC spectrum from the 1992 August 10 observation. This produced a continuum spectrum with α_{ox}, defined here in the standard way as the index of the power law stretching between 2500 Å and 2 keV (e.g., Wilkes et al. 1994), which is 1.63 for IRAS 13224−3809. We note that for 1H 0707−495, a comparison between the *HST* spectrum and the *ASCA* spectrum obtained on 1995 March 15 also reveals $\alpha_{ox} = 1.63$. An average quasar with a logarithm of its luminosity at 2500 Å of 29.3 is expected to have $\alpha_{ox} = 1.4$, with a range for most of the objects that is between 1.06 and 1.64 (Wilkes et al. 1994). Therefore, IRAS 13224−3809 and 1H 0707−495 appear to be somewhat X-ray−weak.

Much of the continuum is not well observed or is unknown, and therefore, we adopt the generic "AGN continuum" included in CLOUDY for the energy bands for which there is no information (Fig. 1). The shape of the spectrum between 2 and 10 keV is not very well defined for these objects because of the complexity of the spectrum and low signal-to-noise ratio. Furthermore, nothing is known above 10 keV. We assume a power law[4] with $\alpha = 1$ between 1.9 and 100 keV and a power law with $\alpha = 1.6$ for energies greater than 100 keV. IRAS 13224−3809 has a large excess of infrared emission compared with the AGN continuum (Fig. 1), but as noted in Paper I this object seems to have a strong galaxy component, and therefore, the infrared emission may be dominated by the starburst. Therefore, we adopt the CLOUDY AGN continuum longward of 4430 Å.

---

[3] We do not know with certainty the geometric and physical origin of the emission lines in the objects we are discussing here. However, for simplicity, we refer to the highly blueshifted high-ionization lines as originating in the "wind," and the narrow, symmetric, low-ionization lines as originating in the "disk."
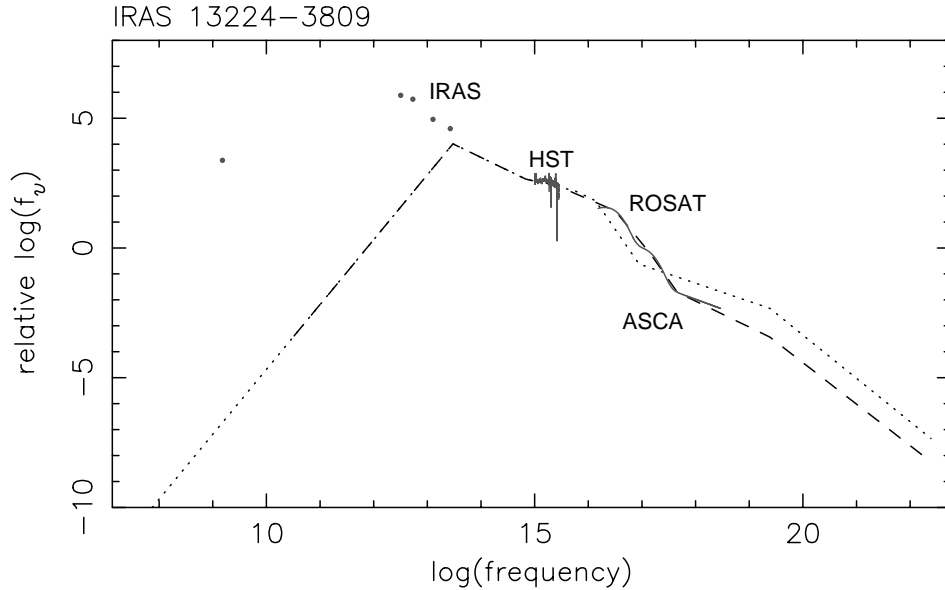
[4] $P(f) \propto f^{-\alpha}$.

FIG. 1.—Adopted continuum for CLOUDY simulations (*dashed line*) constructed from the nonsimultaneous *HST*, *ASCA*, and *ROSAT* observations, and the CLOUDY AGN continuum (*dotted line*).

The *ROSAT* soft X-ray spectrum was rescaled to match the *ASCA* flux level, and power laws with slopes α of 2.5 and 2.96 were used between 0.13–0.58 and 0.58–1.9 keV, respectively. Between 0.011 and 0.13 keV, the spectrum is unknown. Rather than try to guess a spectral shape in this region, initially we simply joined the UV and X-ray spectra, using a power law with slope 0.9. The resulting continuum is shown in Figure 1, compared with the CLOUDY AGN continuum. It is not surprising that the adopted continuum is brighter in the soft X-ray but fainter in the hard X-ray than the CLOUDY AGN continuum.

We also considered three other related continua. For two of the continua, we consider the possibility that the X-ray flux is lower than it was during the *ASCA* observation. This may be justified by the observed high-amplitude variability of these objects and the fact that 1H 0707−495 has been observed in a low state, about a factor of 10 lower than during the *ASCA* observations, in three out of the six epochs of observation since 1990 (Leighly et al. 2002; K. Leighly et al. 2004, in preparation). Furthermore, it is quite possible that if the line-emitting gas has a disklike configuration and lies close to the accretion disk, it may see a continuum deficient in the X-ray. We constructed the X-ray−weak continua by decreasing the X-ray flux by an arbitrarily chosen factor of 4. Since we do not know where the break in the X-ray spectrum occurs in the unobservable extreme UV, we tried two low-flux continua: one called the "low flux (soft)" continuum, in which the *HST* spectrum is directly joined by a power law to the X-ray spectrum, and another called the "low flux (hard)" continuum, in which the slope of the *HST* spectrum is extrapolated to 77 eV, the ionization potential to create N^{+4}, before breaking to the X-rays. These continua are shown compared with the nominal IRAS 13224−3809 continuum in Figure 2.

Finally, it has been proposed that the gas responsible for absorption lines in broad absorption line QSOs (BALQSOs) can be accelerated by radiative line driving if the X-rays are absorbed out of the continuum before they illuminate the absorbing gas (Murray et al. 1995). We therefore also try the IRAS 13224−3809 continuum transmitted through the gas

with $\xi = 200$[5] (which corresponds to $\log U = 0.9$) and column density of 10^{23} cm^{-2}. The ionization parameter of $\xi = 200$ was chosen because it is close to the largest ionization parameter possible with negligible loss of radiation-driving force (Stevens & Kallman 1990). The continuum is shown in Figure 2. Note that when discussing transmitted continua, we report the photon fluxes and ionization parameters *before* transmission.

2.2. *Modeling the Wind Lines*

We next use CLOUDY to compute the emission-line spectrum of the gas subject to this continuum. We concentrate on the following 10 emission lines: Lyα, N v, Si iv, O iv], C iv, He ii, Al iii, Si iii], C iii], and Mg ii.

The intent of the photoionization modeling described in this section and § 2.3 is to use the emission-line ratios and equivalent widths to obtain estimates of the ionization parameter, column density, metallicity, density, covering fraction, and constraints on the illuminating continuum if possible. These results are then used in the subsequent section to constrain the remaining parameters, as well as the distance of the line-emitting gas from the continuum source.

We first investigate the broad blueshifted "wind" lines. Of the 10 lines listed above, broad components of the first six (Lyα, N v, Si iv, O iv], C iv, and He ii) were inferred to be present (measurements are given in Table 2 of Paper I), and the last four were not detected. We assign the upper limit of 5 Å to Al iii, Si iii], and C iii], and an upper limit of 10 Å to Mg ii. Generous upper limits were used because a weak broad component could not easily be distinguished from the continuum.

Six parameters influence the predicted equivalent widths of the emission lines: the ionization parameter, the gas density, the column density, the covering fraction, the metallicity, and the continuum. We have already described the four continua that we consider. We consider three metallicity combinations:

---

[5] ξ is defined by $\xi = L/nR^2$, where L is the luminosity between 1 and 1000 ryd, n is the gas density, and R is the radius (Tarter et al. 1969).
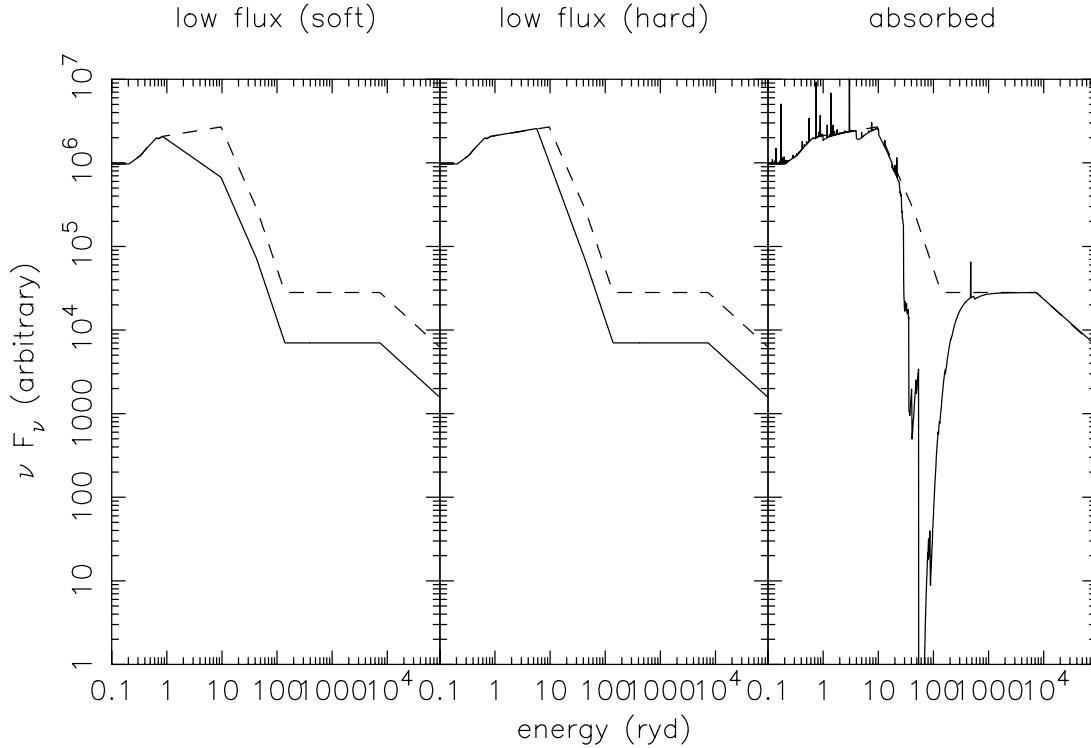
Fig. 2.—Portions of the continua used for modeling the wind, compared in each case with the IRAS 13224−3809 continuum developed from the *HST* and nonsimultaneous *ASCA* and *ROSAT* spectra.

solar; all metals enhanced by a factor of 5 over solar; and all metals enhanced by a factor of 5 over solar, with nitrogen alone enhanced by a factor of 10 over solar. We do not make a complete search of metallicity parameter space because preliminary investigations show that the data cannot constrain the metallicity with high precision; this issue will be revisited when the *HST* spectra of 1H 0707−495 are analyzed in combination with the *Far-Ultraviolet Spectroscopic Explorer* (*FUSE*) spectra (K. Leighly et al. 2004, in preparation). The combinations to present were determined on the basis of preliminary trial-and-error batches of simulations. We made grids of the equivalent widths of the 10 emission lines listed above predicted from CLOUDY runs for the following three parameters, followed by the ranges and intervals that we consider: the logarithm of the density (7.0–12.0 by 0.25); log U (ionization parameter,[6] −3.0 to 0 by 0.25); and log N_H^{max} (21–23.4 by 0.2), where N_H^{max} is defined as log N_H − log U and N_H is the column density. N_H^{max} is a useful parameter for studies of photoionized gas because it adjusts the column density to account for the ionization parameter. Thus, for a particular value of N_H^{max}, we probe to the same depth in terms of elemental ionization fractions regardless of the ionization parameter. The range of ionization parameter explored encompasses the "nominal" value understood for the AGN broad-line region of −2, as well as lower values inferred for NLS1's by Kuraszkiewicz et al. (2000). The range of log N_H^{max} considered spans from gas that is rather optically thin in the continuum through gas that includes the hydrogen ionization front (around log N_H^{max} of 23). The range of densities considered starts just above the

constraint imposed by the lack of an observed broad component of [O III] ($n_{crit} \approx 10^6$ cm^{-3}; Osterbrock 1989) and extends through densities at which the bright permitted lines start to become thermalized (e.g., Kuraszkiewicz et al. 2000). In computing the equivalent width, we explore a range of covering fractions (0.01–0.5 by 0.01).

Initially, our search through these thousands of simulations was made by an iterative process of running simulations, comparing results with the data, understanding why particular solutions did not work, tweaking the parameters, and running more simulations. Finally, however, we devised a less subjective criterion to determine how well the parameters fit the data. We use a figure of merit (FOM) that is defined as the sum of the absolute values of the differences of the logarithm of the equivalent width of the emission lines observed and the logarithm of the emission-line equivalent widths predicted by CLOUDY. The lines considered in the sum are the ones detected in the wind: Lyα, N V, O IV], C IV, and He II. We then exclude from consideration any solutions that exceed the upper limits for the lines not detected in the wind: Al III, Si III], C III, and Mg II. Clearly, the FOM will be small when the predicted equivalent widths are close to the observed values. In this way, it is like a surrogate χ^2; however, FOM is not a proper statistical parameter like χ^2. Thus, we computed the FOM for each simulation, constructing a four-dimensional FOM matrix for each of the 12 combinations of continuum and metallicity. We then searched the FOM matrices for the minimum values of FOM.

There are two ways to think about the combination of parameters that produce low values of FOM. The first way is to look for the solution that produces the absolutely smallest value of FOM. For every combination of continuum and metallicity, the smallest FOM is produced in very high density (log n = 12), very high column (log N_H^{max} = 23.4), and very

---

[6] The ionization parameter U is defined as the photoionizing flux Φ, divided by the density n and c, the speed of light, to make it dimensionless. It can be thought of as the ratio of the photon density, which controls the rate of ionization, to the matter density, which controls recombination.

TABLE 1
WIND SOLUTION RESULTS

Continuum	Metallicity[a]	Minimum FOM	Number of FOM Points below 120	$\log n$[b]	$\log U$[b]	$\log N_{\mathrm{H}}^{\mathrm{max}}$[b]	Covering Fraction[b]
Nominal......................	Solar	75	211	11.75–12.0	−0.6–0.0	23.0–23.4	0.14–0.4
	Metals 5 $Z_\odot$	57	2612	10.0–12.0	−1.4–0.0	22.0–23.4	0.07–0.41
	Metals 5 $Z_\odot$, N 10 $Z_\odot$	11	12049	7.0–12.0	−2.0–0.0	21.4–23.4	0.06–0.48
Low flux, soft	Solar	74	756	11.5–12.0	−0.8–0.0	22.8–23.4	0.2–0.49
	Metals 5 $Z_\odot$	59	4609	8.5–12.0	−1.2–0.0	22.0–23.4	0.18–0.49
	Metals 5 $Z_\odot$, N 10 $Z_\odot$	16	17817	7.0–12.0	−1.6–0.0	21.6–23.4	0.16–0.49
Low flux, hard	Solar	66	600	11.5–12.0	−0.6–0.0	22.8–23.4	0.14–0.47
	Metals 5 $Z_\odot$	61	5722	7.75–12.0	−1.2–0.0	21.6–23.4	0.09–0.49
	Metals 5 $Z_\odot$, N 10 $Z_\odot$	28	18400	7.0–12.0	−1.8–0.0	21.4–23.4	0.09–0.49
Ionized absorber[c]	Solar	76	226	11.5–12.0	−0.6–0.0	23.0–23.4	0.13–0.5
	Metals 5 $Z_\odot$	61	2176	10.75–12.0	−1.4–0.0	22.2–23.4	0.06–0.5
	Metals 5 $Z_\odot$, N 10 $Z_\odot$	12	12454	7.0–12.0	−2.2–0.0	21.2–23.4	0.05–0.5

[a] Metallicity value of "metals 5 $Z_\odot$" means that the metals are assumed to be enhanced by a factor of 5 over solar, and "metals 5 $Z_\odot$, N 10 $Z_\odot$" means that metals are assumed to be enhanced by a factor of 5 over solar and nitrogen alone is enhanced by a factor of 10 over solar.
[b] The range of parameters listed represents 95% of the full range of parameter combinations with FOM < 120.
[c] The ionization parameter listed is the value before transmission through the absorber.

high ionization ($\log U = 0$) gas. This is essentially the solution that Kuraszkiewicz et al. 2000 found, and we discuss the nature of this solution as type I solutions below.

The second way to view the solutions takes a different view of the physical conditions in the emission region. In reality, the line-emitting gas may not be characterized by a *single* value of the parameters, but a *range* of densities and ionization parameters may be present. In this case, we may be more interested in FOM minima that are shallow, implying that combinations of parameters neighboring the FOM minimum should also produce emission lines with equivalent widths and ratios near the observed values. A solution characterized by a broad FOM minimum relies less on fine-tuning than does one with a narrow minimum.

To first explore the FOM minima for the twelve combinations of metallicity and continuum, we list in Table 1 the number of points in the FOM grid that fall below an arbitrarily chosen value of 120, as well as the range of parameters encompassed by FOM < 120. We find that a much larger region of parameter space produces emission lines and ratios close to the observed values when the metallicity is elevated and the X-ray flux is low.

Why are more solutions available for the higher metallicity and lower X-ray flux continua? The reason seems to be the presence of multiple minima in the high-metallicity low–X-ray–flux FOM matrices. We found these multiple minima in two ways. We looked at the distribution of parameters for solutions with FOM < 120. Double peaks in several cases indicated multiple minima. We also looked at histograms of the "distance" of the solutions from the solution characterized by global-minimum FOM, for which the distance was simply defined by the square root of the sum of the squares of the parameter indices. Multiple peaks were found in these histograms, again indicating the presence of multiple minima. We determined the density, ionization parameter, column density, and covering fraction responsible for the different minima by looking at histograms of parameters selected from small ranges in the FOM distances, and we could identify the local minimum by looking at the FOM rank-ordered list of parameters.

We found that the minima could be divided into three different types on the basis of the physical condition of the gas.

To understand the properties of these minima, two plots are presented. Figure 3 shows the logarithm of the ratio of the observed equivalent widths to the predicted equivalent widths for cuts through the equivalent-width matrix that intersect representative examples of the three types of minima. Figure 4 shows contours of FOM up to the value of 120 for planes of $\log n$ and $\log U$, and $\log N_{\mathrm{H}}^{\mathrm{max}}$ and a covering fraction for the same representative minima.

Type I.—High-density, high $N_{\mathrm{H}}^{\mathrm{max}}$. This solution is similar to the ones obtained without the benefit of profile deconvolution by Kuraszkiewicz et al. (2000). The representative case shown in Figures 3 and 4 has the nominal continuum and solar metallicity, and $\log n = 12$, $\log U = 0$, and $\log N_{\mathrm{H}}^{\mathrm{max}} = 23.4$, and the covering fraction is 0.26. The solutions are pegged at the highest values of density, ionization parameter, and column density. As can be seen in Figure 3, the very high density results in some degree of thermalization in such permitted lines as Lyα and C IV, reducing the equivalent widths of these lines. The high column ensures sufficient line emission, especially from lower ionization species, such as Si IV. The high ionization decreases the emission from lower ionization lines.

This solution is rather fine-tuned. It encompasses only a small region of parameter space constrained at high densities, as seen in Figure 4, because lower density gas produces too much Lyα and C IV. Lower ionization parameter gas produces too much C III].

As discussed above, this type of solution always produces the lowest FOM for all combinations of continuum and metallicity. The parameters corresponding to this minimum are nearly the same for the other continua and nominal metallicity. As metallicity is enhanced, the allowed range of ionization parameters decreases because intermediate-ionization lines are stronger; however, the column density constraint is looser because the hydrogen ionization front moves toward lower columns as the metallicity increases.

Type II.— Intermediate density, intermediate column density, and intermediate ionization parameter. This solution is different from type I in that the density is high enough for only Lyα to start to be attenuated by thermalization. The ionization parameter is high enough and the column density is low enough that the intermediate-ionization line upper limit constraint is
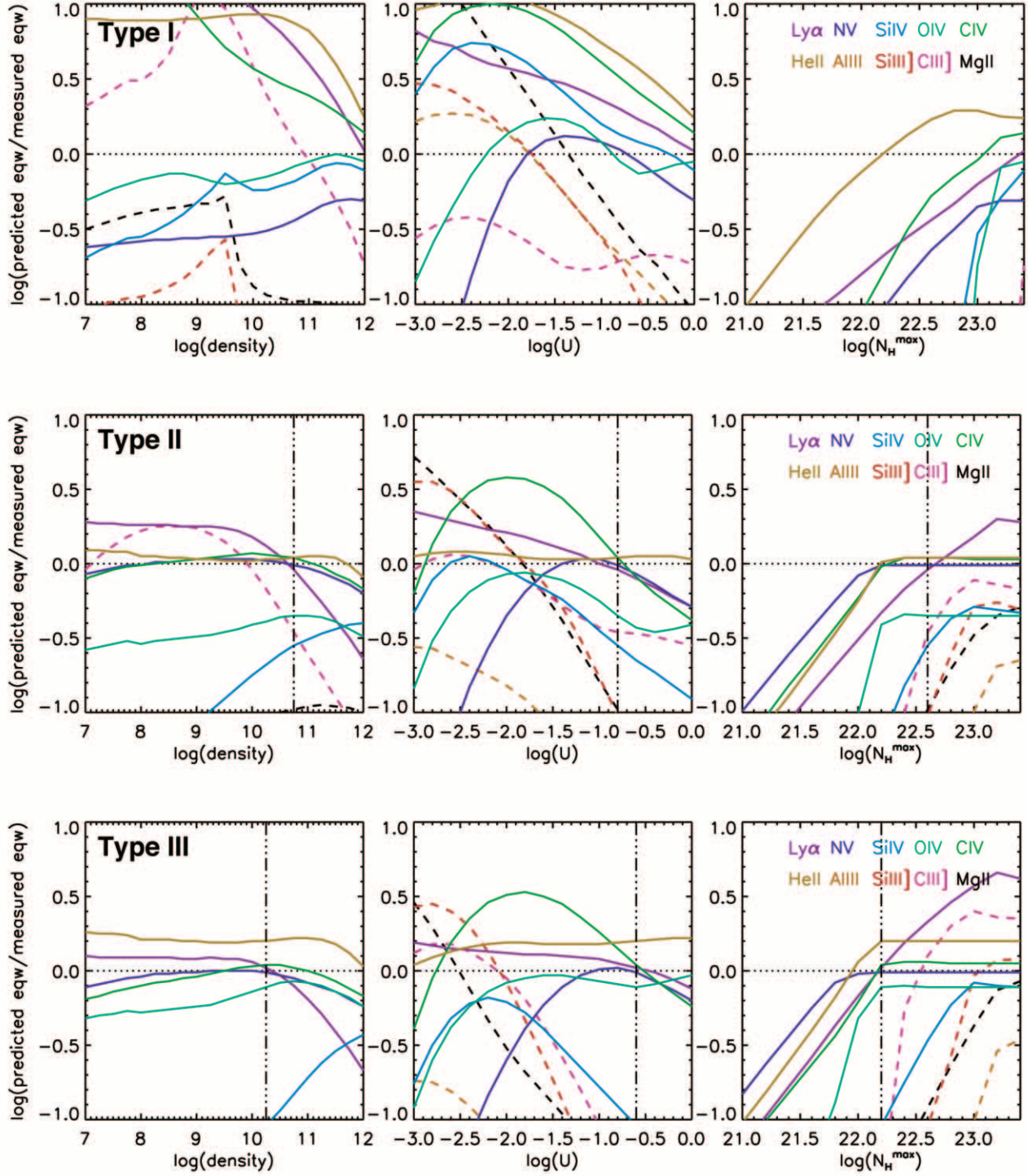
FIG. 3.—Examples of the three representative types of solutions for the photoionization modeling of the wind. The logarithm of the ratio of the observed equivalent width to the predicted equivalent width of Lyα, N v, Si iv, O iv], C iv, and He ii (*solid lines*) and the logarithm of the ratio of the upper limits of the equivalent widths to the predicted equivalents of Al iii, Si iii], C iii], and Mg ii (*dashed lines*) are plotted. The dash-dotted line marks the position of the solution, as follows. The type I representative solution consists of the nominal continuum, solar metallicity, $\log n = 12$, $\log U = 0$, $\log N_{\mathrm{H}}^{\mathrm{max}} = 23.4$, and a covering fraction of 0.26. The type II representative solution consists of the nominal continuum, metals 5 $Z_\odot$ and nitrogen 10 $Z_\odot$ metallicity, $\log n = 10.75$, $\log U = -0.8$, $\log N_{\mathrm{H}}^{\mathrm{max}} = 22.6$, and a covering fraction of 0.08. The type III representative solution has the hard low-flux continuum, metals 5 $Z_\odot$ and nitrogen 10 $Z_\odot$ metallicity, $\log n = 10.25$, $\log U = -0.6$, $\log N_{\mathrm{H}}^{\mathrm{max}} = 22.2$, and a covering fraction of 0.15.

met, and parameter space is constrained sharply toward lower densities and higher column densities by the upper limit on C iii] emission in the wind. The representative solution, shown in Figures 3 and 4, has the nominal continuum, metals 5 $Z_\odot$ and nitrogen 10 $Z_\odot$ metallicity, $\log n = 10.75$, $\log U = -0.8$,

$\log N_{\mathrm{H}}^{\mathrm{max}} = 22.6$, and a covering fraction of 0.08. This solution is found for the nominal, "soft" low-flux continua, and the $\xi = 100$ shielded continua when the metals are enhanced by a factor of 5 over solar and nitrogen is enhanced by a factor of 10 over solar.
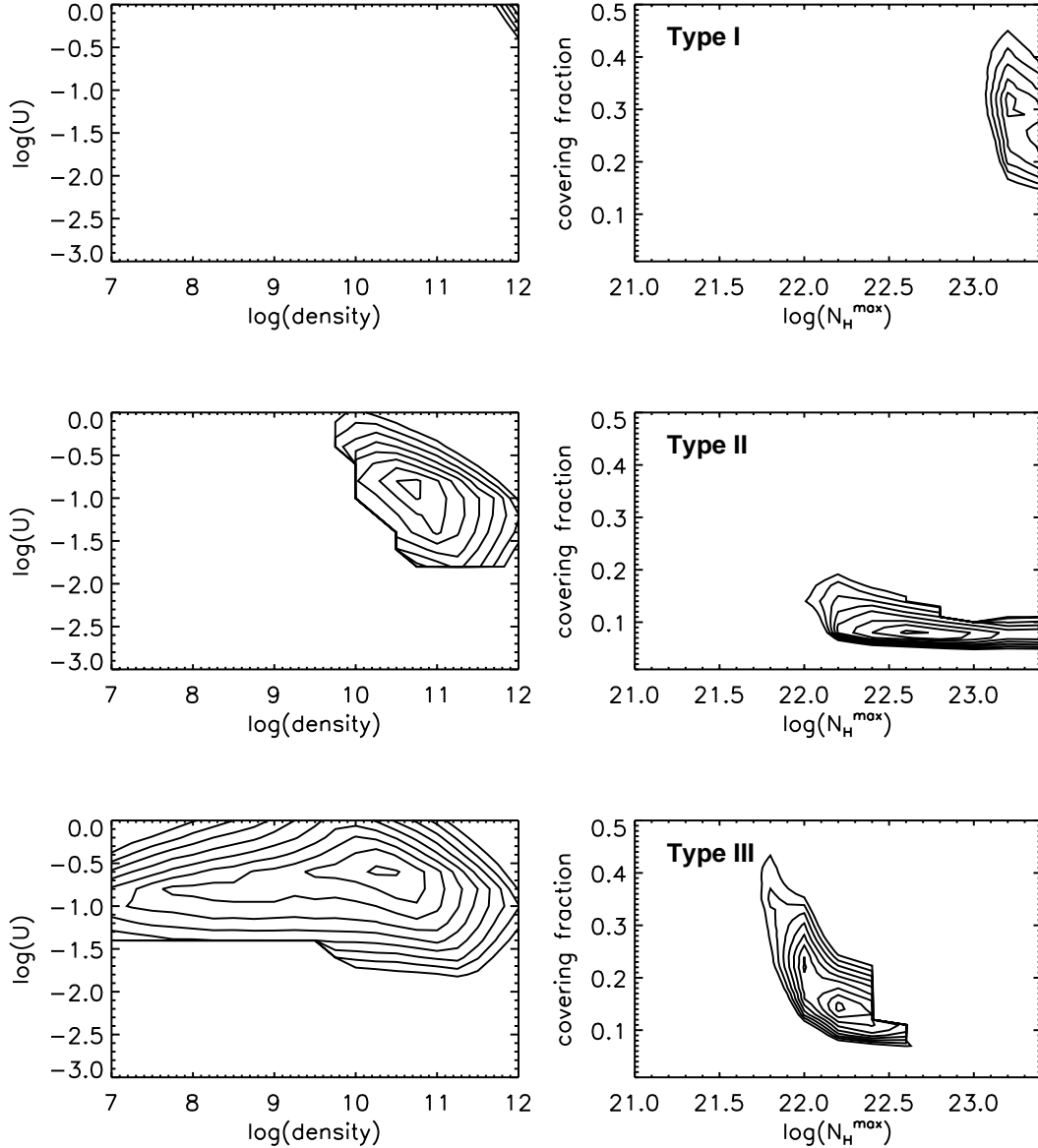
Fig. 4.—Contours of FOM for the three examples of the three representative types of solutions for the photoionization modeling of the wind described in the text and in Fig. 3. In each case, the contour levels are FOM = 0−120 with intervals of 10. The continuum, metallicity, and minimum FOM parameter values are listed in the text and the caption of Fig. 3.

Type III.—Large range of densities, low column density. This solution is different from type II in that a large range of densities, from $\log n = 7$ to ~ 11, is accessible. This is because the relatively low column density truncates the plasma so that no intermediate-ionization lines are produced. Because the column does the job of excluding low-ionization lines, a relatively large range of ionization parameters is also permitted (from $\log U = -1.0$ to 0.0). The representative solution shown in Figures 3 and 4 has the hard low-flux continuum, metals 5 $Z_\odot$ and nitrogen 10 $Z_\odot$ metallicity, $\log n = 10.25$, $\log U = -0.6$, $\log N_H^{\max} = 22.2$, and a covering fraction of 0.15.

It should be noted that for this solution Si IV is not strong enough to contribute to the wind. This is not a problem because, as discussed in Paper I, the 1400 Å feature is composed of both Si IV and O IV], and a robust deblending of these lines was not possible. Therefore, we interpret this result to imply that in the context of this solution the wind contributes only O IV] to the 1400 Å feature.

This solution is found for both the hard and soft low–X-ray–flux continua for the case in which metals are enhanced by a factor of 5 over solar and nitrogen is enhanced by a factor of 10 over solar. Because of the large accessible range of densities and ionization parameters, a very large number of parameter combinations produce an FOM < 120.

We find that the results using the shielded continuum, which has been transmitted through the $\xi = 100$ gas before illuminating the line-emitting region, are almost indistinguishable from the results using the nominal continuum (Table 1). This is because the $\xi = 100$ gas removes photons primarily in the soft X-ray. The soft X-ray photons are not required to create the ions that emit the lines we are considering, nor does their loss represent a substantial loss of energy from the photoionized plasma. We note that the result may have been different had we been considering O VI as well, since O^{+5} has an ionization potential of 113 eV; this will be considered in a future paper. Also, further discussion on the role of shielding is presented in § 4.3.3.

Why do the different continua (nominal vs. low X-ray flux) and metallicities produce such different results? We examine this question through an example shown in Figure 5. Figure 5 (*top row*) shows the equivalent-width contours as a function of density and photon flux for a $N_{\rm H}^{\rm max}$ of 22.4 and a covering fraction of 0.1 for the case of nominal continuum and solar metallicity. These plots are similar to those previously discussed in the context of locally optimally emitting cloud models (Baldwin et al. 1995; Korista et al. 1997). Diagonals on these plots lie along a constant ionization parameter, and thus, the fact that the equivalent-width contours lie along diagonals highlights the primary role of the ionization parameter in determining line emission.

As discussed in Paper I, our two objects are characterized by exceptionally low C IV equivalent widths and correspondingly low C IV–to–Lyα ratios (0.7). Figure 5 (*top row*) shows that C IV is produced optimally for $\log U = -1.7$. The C IV–to–Lyα ratio is 1.2 for this $\log U$, much higher than the observed value. Increasing the column density would increase Lyα; however, that would violate the C III] upper limit for the wind. Instead, since Lyα changes less with $\log U$ than does C IV, we can obtain a lower C IV–to–Lyα ratio by moving off the peak of C IV optimal emission toward either a lower ionization parameter or a higher ionization parameter. The fact that the very high ionization line N V is observed in the wind means that we should move toward a higher ionization parameter. However, moving toward higher $\log U$ to match the C IV/Lyα ratio introduces another problem: we do not have sufficient O IV] and/or Si IV to explain the 1400 Å feature, because the equivalent widths of these lines decrease more rapidly toward higher ionization than does C IV (Fig. 5).

How does changing the metallicity help? This point is investigated in Figure 5 (*second row*), which shows the ratio of the emission lines from a model composed of the nominal continuum, with the metals enhanced by a factor of 5, to the emission lines produced with the nominal continuum and solar metallicity. The column densities for both simulations are chosen to truncate at the same continuum optical depth. We find that modifying the metallicity changes the Lyα and He II little, as indeed it should not. The other emission lines are enhanced toward higher photon fluxes; O IV] is especially enhanced. The reason for this is that the larger metallicity increases the number of ions per hydrogen ion available to remove the energy imparted by photoionization. Thus, the ions responsible for the emission lines that we are interested in survive at higher fluxes rather than make a transition to a higher ionization state, and therefore, they emit at higher fluxes. This effect may be similar to that explored previously by Snedden & Gaskell (1999).

How does changing the shape of the continuum help? This point is investigated in Figure 5 (*third row*), which shows the ratios of the emission lines produced by the hard low-flux continuum to those produced by the nominal continuum, both with solar metallicity. Changing the continuum alters the flux of Lyα and He II little. The other lines are again enhanced toward higher fluxes. The reason for this can be traced to the role of the X-ray continuum as primarily a source of energy in the photoionized gas. The hard low-flux continuum contributes less energy per ionizing photon to the gas than does the nominal continuum. This again allows the ions that are responsible for the emission lines that we are interested in to survive at higher fluxes.

The effect of changing both the metallicity and the continuum is shown in Figure 5 (*bottom row*). In this case, we

also increased the nitrogen abundance to 10 times the solar value to better match the observed N V. Selective enhancement of nitrogen is justified on the basis of secondary enrichment processes that may be important in AGNs (e.g., Hamann et al. 2002). The overall result is that now we can match the observed C IV–to–Lyα ratio at a higher ionization parameter than is optimal for C IV production. At the same time, because of the enhanced cooling due to higher metallicity and reduced heating by the low–X-ray–flux continuum because of the smaller amount of energy per ionizing photon, the O IV] is strongly enhanced, sufficient to explain the 1400 Å feature.

We examine this result in complementary way in Figure 6, which shows the ionization fraction for C^{+3} and O^{+3} as a function of depth into the ionized gas normalized by the depth of the hydrogen ionization front. This figure, similar to those presented by Snedden & Gaskell (1999), supports the assertion presented above. When the metallicity is increased and when the continuum has lower X-ray flux, the O^{+2}/O^{+3} front moves toward the illuminated side of the gas slab relative to the C^{+2}/C^{+3} front, indicating that the O^{+3} ion survives under higher ionization conditions than it does for the nominal continuum and metallicity.

To summarize, the analysis presented in this section shows that three types of combinations of continuum, metallicity, density, ionization parameter, column density, and covering fraction match roughly the observed high-ionization emission lines from the wind without overproducing the intermediate- and low-ionization lines not seen in the wind. We favor the type III solution, characterized by a large range of densities ($\log n \sim 7-11$), a moderate range of fairly high ionization parameters ($\log U \sim -1.2$ to -0.2), a low column density ($\log N_{\rm H}^{\rm max} \sim 22-22.2$), and a moderate covering fraction (0.13–0.25), because it is characterized by a broad minimum in FOM space, so that a large number of combinations of parameters produce the emission-line equivalent widths and ratios that we observe.

2.3. *Modeling the Disk Lines*

We next attempt to determine the properties of the gas emitting the relatively narrow, symmetric, intermediate- and low-ionization lines. Most of the intermediate-ionization lines have profiles consistent with one another, suggesting that they are all produced in the same gas. However, as discussed in Paper I, Mg II and Hβ lines are measurably narrower than the C III], Si III] and Al III emission lines, indicating that they may be produced predominately at larger radii.

To investigate properties of the disk component, we consider the 10 lines used to constrain the wind. As discussed in Paper I, we do not see narrow symmetric components of the high-ionization lines N V, C IV, and He II; therefore, we set upper limits for them. The upper limits for N V and He II are set to 1 Å. This is a tighter constraint than was imposed for the upper limits on lines not seen in the wind, but it is justified by the fact that narrow lines are easier to detect. We have made the simplifying assumption that the C IV line is produced solely in the wind. However, a portion of the C IV profile overlaps that of the disk line C III], and this portion could in principle be produced in the disk. The equivalent width of that overlapping portion of the C IV profile is 4.1 Å, so we take this as the upper limit of C IV produced in the disk component. We also consider the low-ionization lines C II $\lambda1335$ and C II $\lambda2327$, both clearly detected, and N III $\lambda1750$, which is
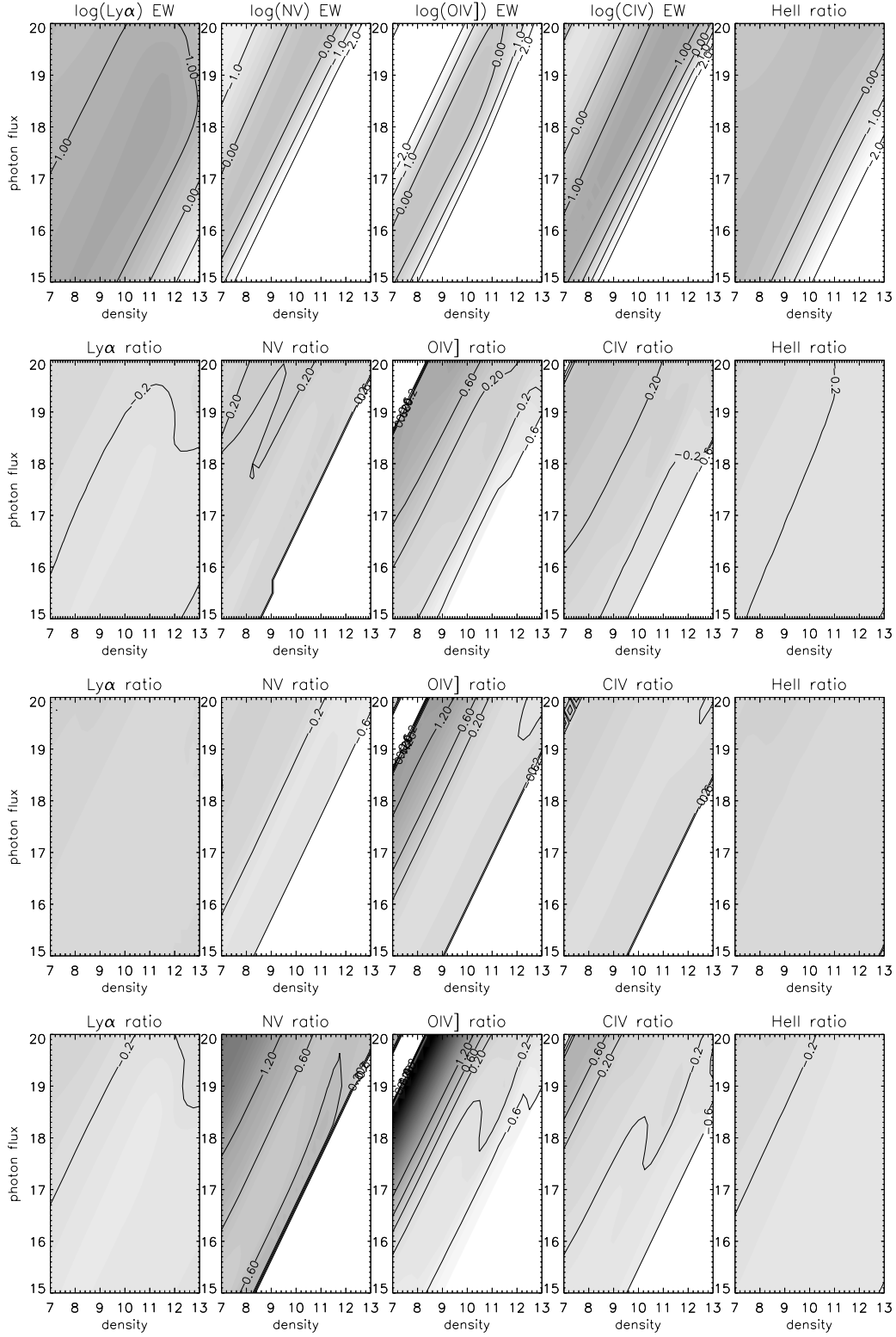
Fig. 5.—*Top row*: Equivalent widths for selected lines for a model consisting of the nominal continuum, solar metallicity, $\log N_{\rm H}^{\rm max} = 22.4$, and a covering fraction of 0.1. *Second row*: Logarithm of the ratio of emission lines for a model having metallicity enhanced by a factor of 5 to those from the model with nominal continuum and solar metallicity. $N_{\rm H}^{\rm max}$ is adjusted so that the fraction of the distance to the hydrogen ionization front is the same in both cases. *Third row*: Logarithm of the ratio of the emission lines for a model having a hard low-flux continuum with solar metallicity to those having a nominal continuum and solar metallicity. *Bottom row*: Combination of results from the second and third rows, showing the logarithm of the ratio of the emission lines for a model having the low-flux (hard) continuum, metals enhanced by a factor of 5 times solar, and nitrogen enhanced by a factor of 10 times solar to those from a model with nominal continuum and nominal metallicity.
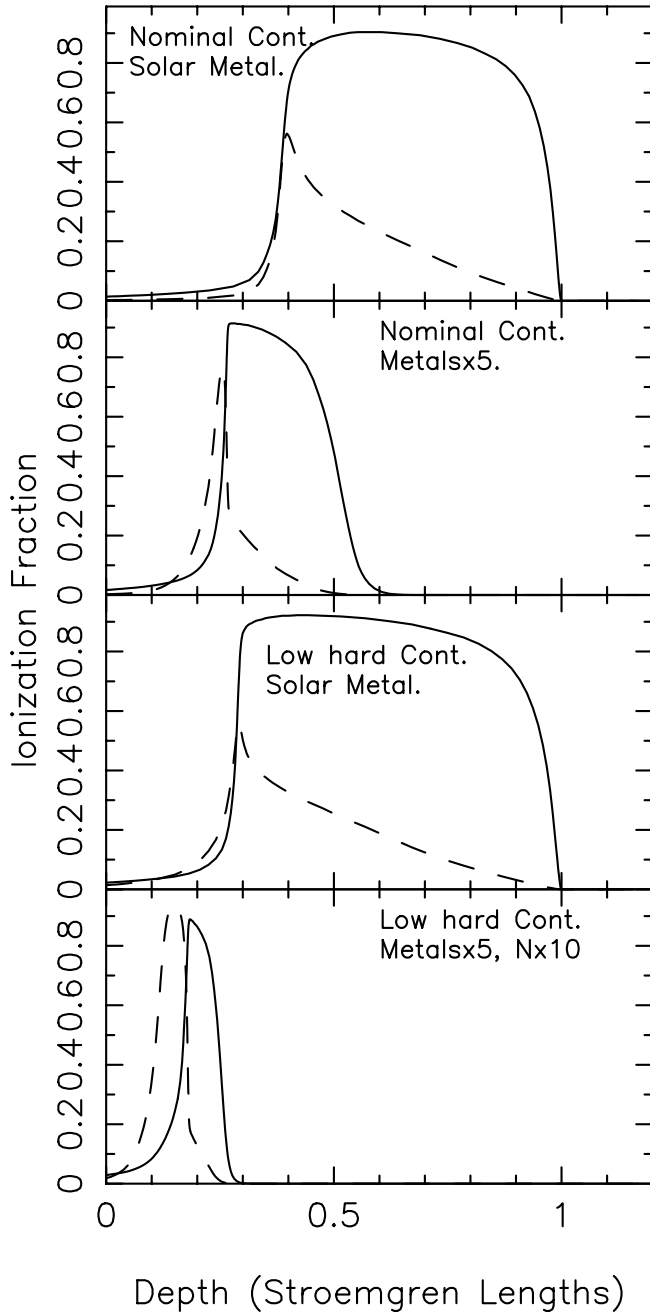
Fig. 6.—Ionization fractions for C^{+3} (*solid line*) and O^{+3} (*dashed line*) for different continua and metallicity, as a function of depth into the ionized gas normalized by the depth to the hydrogen ionization front.

marginally detected at best. We do not use the prominent Si II lines, as it is clear that our spectra suffer "the Si II disaster" (Baldwin et al. 1996); that is, Si II appears to be selectively excited in some way.

We set up the model as follows. We use the results from the previous section and assume the type III solution for the wind, composed of the hard low-flux continuum and enhanced metallicity (metals enhanced by a factor of 5 and nitrogen enhanced by a factor of 10 over solar). In the disk component, we observe lines with quite low ionization, including Mg II, C II, and Si II. These low-ionization species suggest that the column density of the disk component extends past the hydrogen ionization front. We therefore set the column density to be 5 times the depth to the hydrogen ionization front using $N_{\rm H}^{\rm max}$ as before. We also considered higher column densities and found that the results are not sensitive to this parameter; this is expected since most of the lower ionization lines that we consider are produced in the vicinity of the hydrogen ionization front.

In the disk component, we find the intermediate-ionization intercombination lines C III] and Si III]. These lines are very useful for constraining the density of the disk component since they are produced under roughly the same physical conditions (e.g., Hamann et al. 2002), yet they have different critical densities (3.4×10^9 and 1.04×10^{11} cm^{-3}, respectively). Therefore, their ratio provides a density constraint that is fairly independent of the ionization parameter. Requiring the ratio of these lines to be consistent with the observed value of 1.4 and requiring the equivalent widths to match the observed values gives an estimate of the density, the photon flux, and the covering fraction. The density and covering fraction could be constrained rather tightly: they fell between 10.0 and 10.5, and between 0.04 and 0.1, respectively, in all cases (Table 2). To illustrate these solutions, we plot the logarithm of the ratio of the predicted equivalent widths to the measured value or upper limit as a function of the logarithm of the photon flux (Fig. 7).

The primary constraint for the disk lines is the low value of the ratio of the upper limit of the narrow component of C IV to C III] compared with other objects discussed in Paper I. C IV is generally a very strong line. The two objects discussed in detail here are remarkable in that the narrow component of C IV is weak. Following reasoning similar to that presented in § 2.2, we find that to produce the low inferred ratio of C IV to C III] we must move toward lower ionization parameters than that characterized by optimal C IV emission. Thus, avoiding overproduction of C IV places an upper limit on the logarithm of the photon flux of ~17.5. This is illustrated in Figure 7: as the photon flux increases, the predicted flux of C IV increases fairly rapidly and quickly becomes much stronger than that we see.

TABLE 2
DISK PHOTOIONIZATION MODEL PARAMETERS

Continuum	Logarithm of Density	Logarithm of Photon Flux[a]	log U[a]	Covering Fraction
Direct (metals 5 $Z_\odot$, N 10 $Z_\odot$)..	10.0	17.5	−3.0	0.035
Direct (metals 5 $Z_\odot$)	10.0	17.5	−3.0	0.03
Wind-filtered (metals 5 $Z_\odot$, N 10 $Z_\odot$)..	10.25	18.7	−2.1	0.05
Direct (metals 5 $Z_\odot$, N 10 $Z_\odot$) $v_{\rm turb} = 2000$ km s^{-1}	10.0	17.25	−3.2	0.035
Wind-filtered (metals 5 $Z_\odot$, N 10 $Z_\odot$) $v_{\rm turb} = 2000$ km s^{-1}	10.25	18.2	−2.5	0.05

[a] The photon flux and ionization parameter listed for a filtered continuum are the values appropriate for the flux *before* it is transmitted through the absorber.
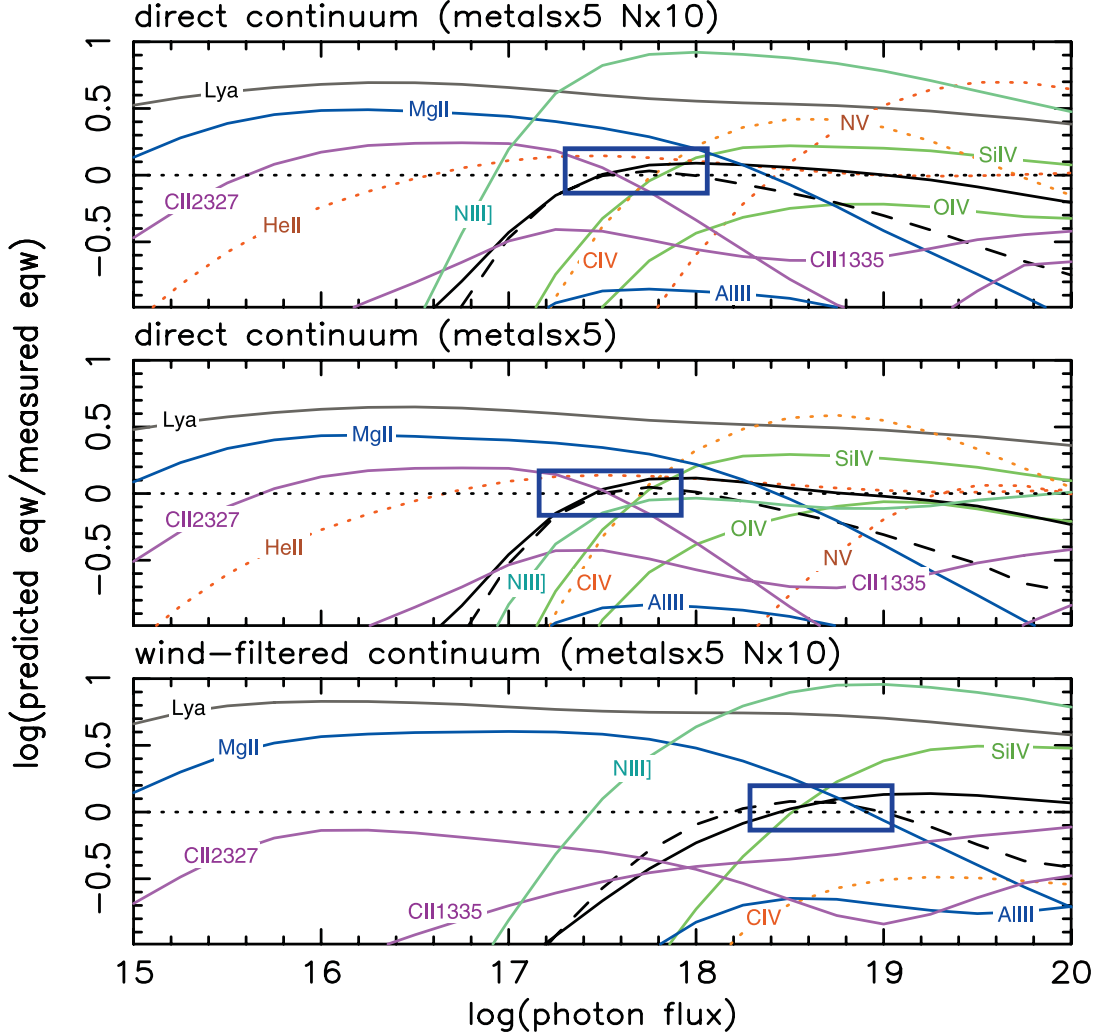
Fig. 7.—Results of photoionization modeling for the disk. The logarithm of the ratio of the model line equivalent widths to the measured equivalent widths are shown. The density and covering fraction were first determined using the equivalent widths of C iii] (*solid black line*) and Si iii] (*dashed black line*) and their ratio, as described in the text. Other lines are marked: solid lines denote detection, and dotted lines denote upper limits. Boxes mark the approximate range of solutions approximately consistent with the observed emission lines.

Kuraszkiewicz et al. (2000) postulated that the low equivalent width of C iv in NLS1's in general arises because the densities are so high that C iv is collisionally de-excited. We find this to be unlikely. As discussed above, the ratio of the semiforbidden lines Si iii] and C iii] provides an estimate of $\log n$ between 10.0 and 10.5. C iv has a critical density of 2.06×10^{15} cm^{-3} (Hamann et al. 2002), and the critical densities of Si iii] and C iii] are several orders of magnitude below that. At densities high enough to de-excite C iv, we would not expect to see any Si iii] or C iii] lines at all. We discuss this point further in § 4.4.

The low inferred photon fluxes imply a very large radius for the emission region. Is there any way it could be smaller? The reasoning presented thus far in this section assumes a one-zone model. But Si iii] and C iii] are produced optimally at lower ionization parameters than is C iv (e.g., Korista et al. 1997). We could imagine, then, a radially extended emission region in which C iv is produced at smaller radii than Si iii] and C iii]. In a disklike geometry, the area of the annulus ($\Delta A = 2\pi r \Delta r$) increases for a given Δr at larger radii, so one could imagine that if we integrate over a range of radii, we would accumulate sufficient C iii], because of the larger area of

an annulus at larger radii, to be able to extend the emission region to smaller radii without violating the constraint imposed by the C iv upper limit to the C iii] ratio. Although a detailed discussion of the implications of a radially extended emission region is beyond the scope of this paper and will be discussed in future work, we make a quick estimation of the viability of this hypothesis here. We simply sum the expected flux from C iv, C iii], and Si iii], weighting the flux as though the emission were from a disk (i.e., $2\pi r \, dr$); perhaps this is appropriate given the very small covering fraction that we infer. We perform this summation for a range of starting radii (corresponding to a range of maximum photon fluxes $\log \Phi_{max}$) to a fixed maximum radius corresponding to $\log \Phi_{min} = 15$. The results, shown in Figure 8, reveal that with one exception, discussed below, regardless of the continuum and metallicity, starting the integration at $\log \Phi_{max}$ larger than about 18 will produce an integrated value of C iv that is too large. Thus, integration over an extended region still requires a very large radius for the emission.

There is another, more viable way to decrease the radius of the emission region that also conveniently explains the relative emphasis on lower ionization emission lines in the disk
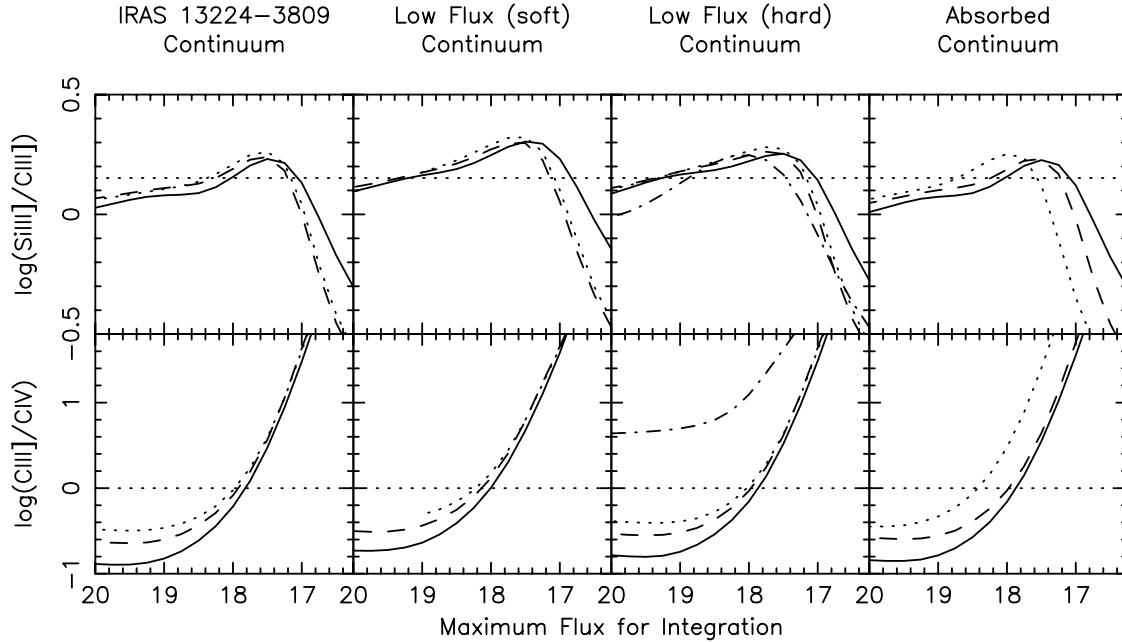
IRAS 13224−3809
Continuum

Low Flux (soft)
Continuum

Low Flux (hard)
Continuum

Absorbed
Continuum

FIG. 8.—Logarithm of the ratios of Si III] to C III] and C III] to C IV for different continua (*left to right*) and for solar metallicity (*solid line*), metals 5 $Z_\odot$ (*dashed line*), and metals 5 $Z_\odot$ and nitrogen 10 $Z_\odot$ (*dotted line*). The dot-dashed line shows the wind-filtered continuum. In each case, the line emission is integrated from the radius corresponding to the flux on the *x*-axis (the minimum radius) to $\log \Phi = 15$ (the maximum radius). See text for additional information. Horizontal dotted lines show the measured value for the Si III]/C III] ratio, and the lower limit for the C III]/C IV ratio.

component. Consider the possibility that the continuum has been filtered[7] through the wind before it illuminates the disk. Filtering the continuum through the wind removes photons in the helium continuum, making the resulting transmitted continuum unable to produce or excite highly ionized ions. We test this possibility as follows. We use CLOUDY to obtain the continuum transmitted through a wind with $\log U = -0.8$ and $\log N_H = 21.4$ and metals and nitrogen enhanced by factors of 5 and 10 over solar, respectively. We use a wind density of $\log n = 9.5$ but note that the shape of the transmitted continuum is not sensitive to this parameter. The value of the ionization parameter of $\log U = -0.8$ was chosen because it is characteristic of a large region of wind parameter space for the type III solution (Fig. 4). The transmitted continuum is shown in Figure 9. As expected, this continuum is severely deficient in photons above the helium edge at 54 eV, and therefore, it is neither able to create highly ionized ions nor able to excite them. We then used this continuum to illuminate the intermediate- and low-ionization line-emitting gas and follow the same analysis of the CLOUDY simulations as above. The results are shown in Figures 7 and 10, and parameters are listed in Table 2. We note that, as before, we report the ionizing flux before transmission through the wind to use the parameters for distance estimation in § 4.1. The net effect of the filtering is to make the continuum quite a bit softer than the unabsorbed continuum. The result is a decrease in the higher ionization lines and an increase in the lower ionization lines. Thus, C IV is quite a bit weaker overall, which means that we find the best correspondence between observed and predicted

equivalent widths at a significantly higher ionizing flux than before ($\log \Phi \approx 18.7$, corresponding to $\log U = -2.1$).

In both cases, we find the predicted value of the equivalent width of Mg II to be about a factor of 3 higher than observed. As discussed in Paper I, the Mg II line is narrower than the C III] and Si III] lines. Therefore, it is probably produced primarily at larger radii. However, that does not alleviate the problem that a substantial amount of Mg II is predicted to be produced in the same gas that emits Si III] and C III], and that is simply not seen. Kuraszkiewicz et al. (2000) also found Mg II to be too strong; this seems to be a generic problem for Mg II. It is possible that the predicted Mg II is affected by the approximate treatment of radiative transfer in CLOUDY, although because Mg$^+$ is a very simple ion, this appears to be unlikely. It is possible that the gas producing the intermediate-ionization lines Si III] and C III] is not optically thick in the continuum and that the column density of the gas is truncated so that little Mg II is produced in the same region as Si III] and C III]. Another possibility is that dust may be present at large radii, and it may soak up some of the resonance-line emission. Further investigation of this issue is beyond the scope of this paper.

Lyα is also too strong by a factor of 3–4. We note that Lyα is very optically thick, and it may also suffer some problems with radiative transfer. In particular, we have already found evidence that Lyα pumps Fe III in some objects (Paper I), and Lyα may also pump Fe II (e.g., Sigut & Pradhan 2003). These mechanisms serve as sinks of Lyα. Lyα would also be severely effected if dust were present. Further investigation of this issue is beyond the scope of this paper.

As discussed in Paper, I, the 1400 Å feature is composed of Si IV and O IV], with contributions from both the disk and from the wind. Figure 7 shows that the simulated Si IV is nearly as strong as observed at our best value of the photon flux but that O IV] is more favorably produced at higher photon fluxes and is therefore too weak. Therefore, we infer that the disk part of

---

[7] Henceforth, we differentiate between a shielded continuum, which is assumed to have been transmitted through highly ionized gas (e.g., Murray et al. 1995), and a "filtered" continuum, which is assumed to have been transmitted through the wind while ionizing and exciting it before illuminating the disk and producing the observed intermediate- and low-ionization lines.
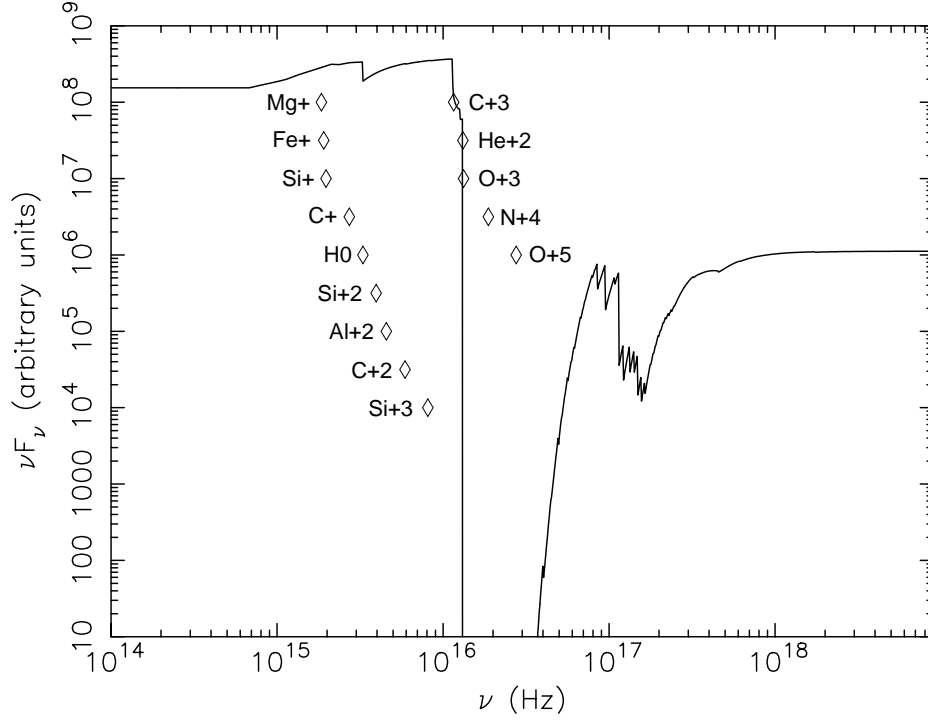
FIG. 9.—Filtered continuum, produced as a result of transmitting the hard low-flux continuum through the wind, showing the frequencies corresponding to the ionization potentials of various ions and the lack of emission in the helium continuum.

the 1400 Å feature is predominantly Si IV, and the broad part is predominately O IV], as discussed in § 2.2.

Al III is too weak in both models; however, it is a factor of only 3 too weak when the continuum is filtered through the wind. This is to be expected: Al III increases as the spectrum becomes globally softer (Casebeer & Leighly 2004). A few test

runs show that it could be enhanced further by a differential increase in density with depth into the slab. The increase in density lowers the ionization parameter, increasing the lower ionization lines that are strong in these objects. Another possibility is that the disk is heated by some mechanism other than photoionization, which might cause the hydrogen ionization
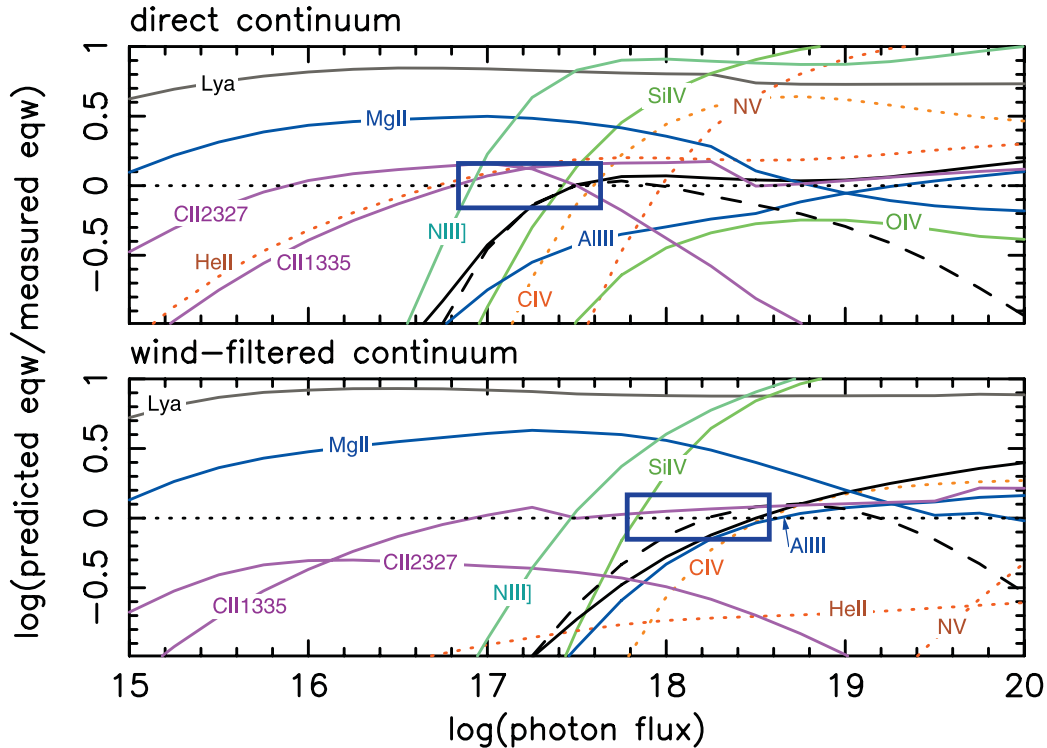

FIG. 10.—Same as Fig. 7 (*top and bottom*), but for a turbulence of 2000 km s^{-1}.

front to retreat farther back into the slab, allowing stronger intermediate-ionization lines.

The ratio of N III] $\lambda 1750$ to C III] is considered to be a good indicator of the relative nitrogen abundance because these two lines are produced under the same conditions (Hamann et al. 2002). The measured value of N III], only marginally identified in the spectrum of IRAS 13224−3809, is roughly consistent with the predicted value for solar metallicities and for metallicity enhanced by a factor of 5 at our best value of ionizing flux (Fig. 7). However, when the nitrogen is selectively enhanced to 10 times solar, the predicted emission from N III] is much too strong, by up to a factor of nearly 10 (Fig. 10). Thus, we find that while the wind lines require nitrogen to be selectively enhanced by secondary enrichment, no such enhancement is required for the disk lines. This may imply that N v in the wind is being selectively excited. It may be pumped by Lyα, a process that would seem to be favorable in a wind because of the large velocity spread and the resulting line overlap. Hamann & Korista (1996) investigated this situation and concluded that it was not important for the average quasar, but the results presented here perhaps suggest that this issue should be revisited for windy quasars in particular. It is also possible that we have not deconvolved the spectrum near Lyα and N v completely accurately. O v at 1218 Å appears in the spectrum of RE 1034+39 (Casebeer & Leighly 2004); we do not model it here, and therefore, we may be overestimating the flux of N v. However, CLOUDY simulations show that O v is likely to be on the order of 1/7.5 times as strong as N v. Furthermore, that component is likely to blend with the Lyα rather than N v. This issue will be discussed further in a forthcoming paper on the *FUSE* spectrum of 1H 0707−495 (K. Leighly et al. 2004, in preparation).

We observe moderately strong features at least partially attributable to Si II $\lambda 1260$, Si II $\lambda 1305$, and C II $\lambda 1335$ (Fig. 2 in Paper I). Such strong Si II features have also been observed in the NLS1 prototype I Zw 1 (Laor et al. 1997b) and other narrow-line quasars (Baldwin et al. 1996). Recently, Bottorff et al. (2000) have shown that these emission lines are predicted to be enhanced under conditions of turbulence. We note that a very large turbulent velocity is probably not warranted in these objects for two reasons. First, the intermediate-ionization lines are observed to be rather narrow (although a distribution in turbulent velocities may mask the broadening effect; M. Bottorff 2001, private communication). Second, the width of the lines is thought to be related to the Keplerian velocity, which is of the same order as the free-fall velocity and represents the reservoir of gravitational energy in the system. Then, the question of the origin of the energy for very large turbulent velocities arises since it should be equal to or less than the equipartition energy of the gravitational field. Therefore, we examine the possibility that the gas is experiencing turbulence with velocities of 2000 km s^{-1}. The primary effect of the turbulence is to reduce the opacity to resonance lines that are usually just optically thick, and therefore, it is possible that the same effect would be observed if there was a mild velocity gradient, as might be expected in a disk, rather than turbulence.

The results are shown in Figure 10. Compared with the directly illuminated disk, we find that Si IV, Al III, and C II increase rather dramatically. This is expected because these lines are formed deep within the slab, near the hydrogen ionization front, and turbulence has reduced their opacity the most. However, C IV is still strong, so we are still constrained to ionizing fluxes of ∼17.5. For the wind-filtered continuum,

we find a similar increase in Si IV and Al III. However, now C IV again increases strongly with flux, and therefore, we are constrained to ionizing fluxes less than about ∼17.5. We conclude that turbulence (or a velocity gradient originating in another type of motion) helps to increase the flux of Al III, which is underproduced in the static models, but then a large radius for the emission region is required.

To summarize, we find that approximate solutions for the intermediate- and low-ionization disk lines can be provided by gas that is optically thick to the continuum, with $\log n$ between 10 and 10.25 and covering fraction between 0.035 and 0.07, assuming that the continuum and metallicity are the best values obtained from the wind modeling. The low observed ratio of narrow C IV to C III] constrains the photoionizing flux to be less than about $\log \Phi \approx 17.5$, if the gas is illuminated directly by the continuum. That value increases to $\log \Phi \approx 18.7$ if the continuum is filtered through the wind before it illuminates the disk. Thus, we infer ionization parameters $\log U$ of −3 for direct continuum and −2.1 for filtered continuum. Then, the logarithm of the column densities we infer are 20.7 and 21.7, although we note that because the gas is ionization bounded, larger column densities are not ruled out and in fact may be supported by observation of NaD (Thompson 1991) in IRAS 13224−3809. Mg II and Lyα are too strong; we speculate that part of the reason for this may be incomplete modeling of the radiative transfer. Al III is somewhat too weak, although not seriously for the filtered continuum; this may indicate that the density of the disk increases with depth or that there is some turbulence or other motion in the disk. N III] is too strong; this may indicate that we overestimate the nitrogen abundance in the wind, possibly indicating selective excitation of the wind line N v by Lyα.

3. ROUGH ESTIMATES OF GEOMETRY AND KINEMATICS

In this section, we use the results of the photoionization modeling and a simple toy dynamical model to make very rough estimates of the size scales and geometry of the wind and the disk components. Our photoionization modeling is simplified, and the dynamical model presented here is very simple as well and cannot be considered a complete model of the quasar by any means. Nevertheless, this exercise is worthwhile because it allows us to obtain quantitative results that can be used to direct development of more complex models.

First, we make two estimates of the black hole mass. The Eddington luminosity is a fiducial parameter of the system; therefore, for the first black hole mass estimate we assume that the quasar is radiating at the Eddington luminosity. We use cosmological parameters $H_0 = 50$ km s^{-1} Mpc^{-1} and $q_0 = 0.5$. We integrate the continua from 1 eV through gamma rays and find that the bolometric luminosity is plausibly bracketed between 2.2×10^{45} and 1.5×10^{45} ergs s^{-1} for the nominal and the soft low-flux continua, respectively. Setting the bolometric luminosity equal to the Eddington luminosity, we obtain a black hole mass estimate between 1 and 2×10^7 solar masses. The Schwarzschild radius for a 1.5×10^7 solar mass black hole is 4.4×10^{12} cm.

The second black hole mass estimate is based on the photoionization modeling performed in § 2.3. The photoionization modeling results are possibly the least model dependent for the C III] line−producing region because of the good density constraint provided by the Si III]–to−C III] ratio. As discussed in § 2.3, when we assume that the continuum is

transmitted (filtered) through the wind before it illuminates the intermediate-ionization line-emitting region, we obtain $\log n = 10.25$ and $\log \Phi = 18.7$, yielding an estimate of the ionization parameter of $\log U = -2.1$. By itself, Φ yields an estimate of the distance to the emission region of 5.3×10^{17} cm. As discussed in Paper I, the FWHM of the C III] line from IRAS 13224−3809 is 1835 km s^{-1}. The FWHM velocity of 1835 km s^{-1} corresponds to $\sigma_v \approx$ FWHM$/2.35 = 780$ km s^{-1}. If the emission region is flattened, the velocities may be larger, in which case we can use the effective velocity dispersion $\sigma_v^2 = 3/4 v^2 C$, or $\sigma_v = 1590$ km s^{-1} (e.g., Wandel et al. 1999). This velocity dispersion yields a black hole estimate of 1.0×10^8 $M_\odot$. Then, using the calibration of the photoionization and reverberation methods proposed by Wandel et al. (1999), we obtain a black hole estimate of 1.3×10^8 $M_\odot$. This is the value that we finally use; we discuss other black hole mass values in the Appendix. The Schwarzschild radius for $M_{\rm BH} = 1.3 \times 10^8$ $M_\odot$ is 3.8×10^{13} cm, and we infer the object to be radiating at 9%–14% of the Eddington luminosity.

3.1. Inferences about the Disk

In this section, we use the photoionization results and the black hole mass estimates to infer the radius of the intermediate-ionization line-emitting region in Schwarzschild radius units. We assume that the continuum illuminates the intermediate-ionization line–emitting region after it is transmitted through the wind; this seems a most promising way to produce the strong low-ionization line emission observed in NLS1's. Then, the photoionizing flux is $\log \Phi = 18.7$, and the distance to the emitting region is 5.3×10^{17} cm, which corresponds to $120{,}000 R_{\rm S}$ and $14{,}000 R_{\rm S}$ for the small and large black hole masses, respectively. Interestingly, these numbers fall approximately within the range of radii for which the accretion disk is predicted to break up because of self-gravity and at which at least part of the line emission may occur (Collin & Huré 2001).

The small black hole mass may not be favored if the velocities of the intermediate-ionization line-emitting region are of the order of the Keplerian velocity or larger and if the emitting region is flattened. The Keplerian velocity at $120{,}000 R_{\rm S}$ is 610 km s^{-1}. When we use $\sigma_v^2 = 3/4 v_{\rm FWHM}$, this corresponds to $v_{\rm FWHM} = 700$ km s^{-1}, a factor of 2.6 smaller than the observed width of C III]. The larger black hole mass does not have this problem, naturally, since the velocity at the line-emitting region is built into the estimate.

There are a few possible ways to make the small black hole estimate more plausible. For example, it is possible that the line width arises partially in Keplerian motion and partially in turbulence. However, turbulence is unlikely to account for a very large portion of the line width because that would require turbulent velocities in excess of Keplerian velocities and therefore far from equipartition with the gravitational energy provided by the black hole. If the lines are emitted at the point where the disk is breaking up, the relevant energy is provided by the self-gravity, but if they are emitted at the breakup point, that should be just about equal to the black hole gravity, although the mass of the accretion disk may also be important (Huré 2002).

It is possible that the gas emitting the intermediate- and low-ionization lines sees a lower flux than we do. Laor & Netzer (1989) show that the ionizing flux has a nearly $\cos \Theta$ dependence (their Fig. 8) for nonrotating black holes. This may be important if the disk-line emission region has a flattened distribution. A flattened distribution would be consistent with the small covering fraction, of order 5%, that we derive from the photoionization modeling. This small covering fraction would then account for the factor of $\sin(0.05\pi/2.0) = 0.078$ reduction in the flux, allowing the emission region to have a factor of 3.6 smaller radius.

Another possibility is that the flux is attenuated in some way before reaching the emission region. We are already assuming that the continuum is filtered through the wind before illuminating the line-emitting gas. Further shielding, or absorption of the soft X-rays in highly ionized gas, a mechanism suggested by Murray et al. (1995) to prevent overionization of the disk wind, is unlikely to help very much. This is because the steep photon flux spectrum means that most of the photoionizing photons are found just past 13.6 eV. This issue is discussed further in § 4.3.3.

To summarize, we infer that if the black hole has a relatively small mass the line-emitting region must see lower flux than we do to reconcile the ionization parameter of the intermediate-ionization lines with their velocity width and to place it securely at a smaller radius than the disk breakup radius. This may happen naturally if the emission region is near the plane of the disk, as might be suspected from the small covering factor. On the other hand, if the black hole mass is larger, as inferred from the black hole mass estimate using the Wandel et al. (1999) calibration of the photoionization and reverberation techniques, the ionization parameter and velocity width are automatically consistent, and the predicted radius is consistent with a location interior to or on the order of the disk breakup radius ($\sim 14{,}000 R_{\rm S}$).

3.2. Inferences about the Wind

We next consider constraints on the wind lines. Here we assume that the wind is best described by the type III photoionization solution for the reasons discussed in § 2.2. Thus, we assume enhanced metallicity (metals a factor of 5 and nitrogen a factor of 10 over solar) and the hard low-flux continuum. A set of parameters representative of the broad FOM minimum illustrated in Figure 4 includes $\log U = -0.8$, the column density $\log N_{\rm H} = 21.4$, and the covering fraction ~ 0.15 (Fig. 4). However, the density for this solution is only loosely constrained at best. Without the density, we cannot estimate the distance of the wind emission from the central engine. Therefore, in this section we use a toy dynamical model to roughly constrain the distance and density.

The toy dynamical model is set up as follows. We assume that radiative line driving is responsible for the acceleration. Radiative line driving is discussed by a number of authors, especially in the context of stellar winds (e.g., Castor et al. 1975, hereafter CAK). We note that the scenario presented here is somewhat similar to that proposed by deKool & Begelman (1995) for BALQSOs. We follow the discussion by Arav & Li (1994) and Arav et al. (1994, hereafter ALB), using our observational parameters to constrain the model.

We postulate that the wind lines are produced in filaments that are accelerated by radiation pressure. Filaments need to be confined even if they are transient. Filaments can be confined thermally or nonthermally. In active galaxies, the predominant confinement mechanism is unlikely to be thermal. That is, the filaments are unlikely to be embedded in a hot gas substrate, for many reasons that have been discussed previously (e.g., Mathews & Ferland 1987). Rees (1987) showed that a nonthermal confinement mechanism may be plausible. Specifically, a magnetic field may confine the filaments, and we adopt this scenario here. Rees (1987) demonstrates that there should

be sufficient magnetic pressure to confine clouds with densities of $n = 10^{10}$ cm^{-3} at distances of 10^{18} cm for objects with quasar luminosity. Our favored densities are about 2 orders of magnitude lower at a slightly smaller distance (see below), so there should be sufficient magnetic pressure to confine the filaments.

We use a highly simplified model to constrain the density and radial distance from the kinematics. We solve the equations in one (radial) dimension; that is, after the gas leaves the disk, it travels in a straight line. We neglect the Keplerian motion that the gas will have as it leaves the disk. These assumptions prevent us from predicting line profiles. Our treatment is arguably complementary to that of, e.g., Proga et al. (2000), since we neglect detailed dynamics but explicitly include constraints from the photoionization modeling. An alternative approach that we plan to investigate in the future is the one used by Kramer et al. (2003), who use the profiles of emission lines in a hot star to derive the wind parameters.

We use the continuity equation, $\dot{M} = 4\pi r^2 \epsilon \rho v(r)$, where $\dot{M}$ is the outflow rate, r is the radius, ϵ is the volume-filling factor, ρ is the mass density, and $v(r)$ is the velocity. We assume that ρ is approximately $m_H n$, where n is the number density.

The momentum conservation equation is $v \, dv/dr = (1/\rho) \, dp/dr - GM_{BH}/r^2 + a_{rl}$, where p is the pressure and M_{BH} is the black hole mass, so GM_{BH}/r^2 is the acceleration in the gravitational field of the black hole, and a_{rl} is the acceleration due to line driving. As pointed out by ALB, acceleration due to the pressure gradient should be small, and we drop that term. We retain the gravitational acceleration term. ALB consider also acceleration due to continuum driving, but they show that it is generally several orders of magnitude weaker than the line driving, so we do not consider the continuum acceleration term here.

The acceleration due to line driving is conventionally written $a_{rl} = (n_e \sigma_t F / \rho c) M_L(U, t)$, where F is the photon flux (e.g., CAK), which depends on the radius according to $1/r^2$. Again, we approximate $\rho/n_e = m_H$. Thus, a_{rl} can be understood to be the acceleration due to electron scattering times the enhancement due to the greater efficiency of resonance-line scattering that is conventionally known as the "force multiplier." The force multiplier, $M_L(U, t)$, depends on the ionization state of the gas, U, since if the ionization is too low or too high, there will be insufficient resonance line–absorbing ions to scatter the photons and absorb their momentum. It also depends on an effective optical depth parameter $t = \sigma_T \epsilon n_e v_{th} (dv/dr)^{-1}$, where v_{th} is the thermal velocity of the gas, which is typically 10 km s^{-1} in photoionized gas. As discussed by Arav & Li (1994) and ALB, this parameter effectively measures the optical depth within a Sobolev length $v_{th}/(dv/dr)$. For gas that has a finite filling factor $\epsilon < 1$, this value is reduced relative to the conventional value. Arav & Li (1994) give a table of M_L as a function of U and t. Those values are computed for the Mathews & Ferland (1974) continuum, which is different from our continuum. However, those values should be approximately appropriate, except for the fact that our enhanced abundances should increase the force multiplier. Thus, while computation of $M_L(U, t)$ is straightforward, it is beyond the scope of this paper.

The acceleration equation can be easily integrated. We assign the integration constant such that $v = 0$ at $r = r_f$. The quantity r_f is referred to as the "footpoint" of the flow by Murray et al. (1995), and we adopt that terminology here. The result is $v^2 = c^2 (R_S/r_f - R_S/r)[M_L(U, t)(L/L_{Edd}) - 1]$.

We assume that once the gas leaves the disk, it continues in a straight line. We assume that the angle between the observer (assumed to be along the symmetry axis) and the streamline is Θ.

We use $M_L(U, t)$ to provide the constraint on the physical parameters of this model, as follows. The velocity law rises quickly to a terminal velocity. We observe a maximum velocity of about 10,000 km s^{-1}. However, that represents only the component of the flow parallel to our line of sight, and therefore, the terminal velocity is assumed to be 10,000 km s^{-1} divided by cos Θ. Given an input footpoint r_f and an Eddington ratio L/L_{Edd}, we can solve for the $M_L(U, t)$ necessary to produce that terminal velocity. Then, we use the best log U, inferred to be -0.8 as discussed in § 2.2, and derive t using other considerations as discussed below. We then require self-consistency: we find the radius at which the value of $M_L(U, t)$ tabulated by Arav & Li (1994) is consistent with the value required to obtain the terminal velocity.

We assume for the purpose of solving the equations of motion that log U stays the same throughout the flow. Assuming that the ionizing photons are isotropic, we can express the density as $n = Q/4\pi r^2 Uc$, where Q is the number flux of ionizing photons.

Next, we find the filling factor $\epsilon(r)$ from the continuity equation. For convenience, we parameterize the outflow rate in terms of the mass accretion rate, which we obtain from $L = \eta \dot{M} c^2$, assuming that the efficiency of conversion from gravitational potential energy to radiation, η, is 10%. Thus, $\dot{M}_{acc}$ is the accretion rate for gas reaching the last stable orbit. We define the parameter $\Gamma \equiv \dot{M}_{wind}/\dot{M}_{acc}$, the ratio of the outflow rate to the accretion rate. We note that the outflow rate can be greater than the accretion rate ($\Gamma > 1$). This just means that not all the gas accreting from infinity actually approaches the last stable orbit and accretes onto the black hole; some is blown out as a wind at a relatively large radius.

At this point, we can also apply our final physical constraint. We found the best estimate of the column density of the flow to be log $N_H = 21.4$. We can integrate $\epsilon(r)n(r)$ over r to obtain the column density. But first we consider the line profile. Because we impose the constraint that the ionization parameter is constant along the flow, the line emissivity per unit radius is proportional to $\epsilon n r^2$. Along a single streamline, this is a steeply decreasing function of $r > r_f$, as a consequence of the continuity equation. This means that most of the mass is at low velocities; however, the profile we see is peaked not at zero velocity but rather at ~ 2500 km s^{-1}. This means either that our admittedly simple velocity law is not sufficient to describe the wind or that the gas at zero velocity must not be emitting significantly; below, we discuss why the low-velocity gas might not be emitting. Regardless, it means that to obtain the column density, we do not integrate the flow from r_f but rather from $r > r_f$, where v is larger than zero. We choose, rather arbitrarily, the lower limit on the integral to be the radius at which the observed velocity $v \approx 2000$ km s^{-1}. For the upper limit of the integration, we consider that at some radius the clouds finally give in and evaporate. We choose the final radius to be that for which the observed velocity is 8000 km s^{-1}, which may be considered the largest velocity at which a significant amount of emission is seen. Then, for a given r_f and $l_{Edd} = L/L_{Edd}$, we can adjust Γ until the calculated column density matches the measured value.

There are a couple of ways that the gas could conceivably be accelerated from zero velocity in such a way that we would not see it initially in the wind. For example, the low-velocity
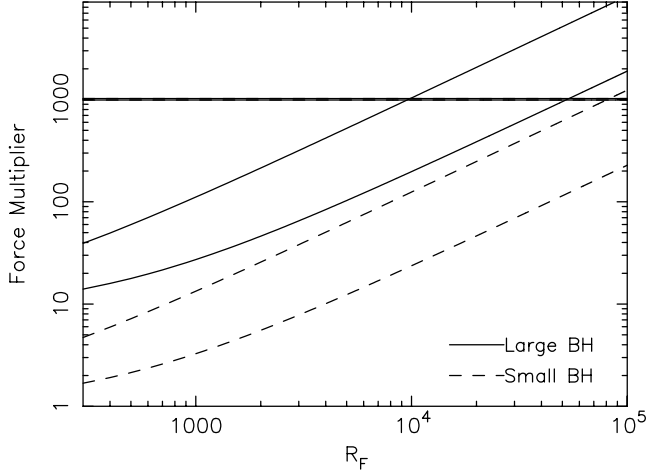
Fig. 11.—Kinematic solutions for the wind, showing the force multiplier (*diagonal lines*) required to attain a terminal velocity projected onto the symmetry axis of 10,000 km s^{-1} and corresponding to the large and small black hole masses (*solid and dashed lines, respectively*). For each assumed black hole mass, the upper and lower lines correspond to the cosine of the streamline angle with respect to the symmetry axis of 0.3 and 0.7, respectively. The horizontal lines represent the values of the force multiplier implied by the physical state of the gas. The point where the two force multipliers cross is a self-consistent solution.

Fig. 12.—Model results for $L/L_{\rm Edd} = 0.12$ and the hard low-flux continuum as a function of $\cos \Theta$, where Θ is the angle between the symmetry axis and the wind streamlines. *Top*, Footpoint radius and the radius at which the projected wind velocity reaches 5000 km s^{-1}, as a function of the Schwarzschild radius for a 1.3×10^8 $M_\odot$ black hole; *second*, density of the outflow; *third*, filling factor for the outflow; *bottom*, $\dot{M}_{\rm wind}/\dot{M}_{\rm acc}$, assuming that the covering fraction obtained from photoionization modeling is 0.15 and that the efficiency of conversion of gravitational potential energy to radiation is 10%.

gas could be accelerated by the continuum but not excited by it. That would be true if the spectrum incident on the lowest velocity gas, presumably closest to the gas source, is transmitted through gas that is optically thick at the Lyman edge. Such a continuum is a primary assumption in the model developed by Proga et al. (2000). Then, as the gas reaches higher and higher velocities, it is exposed to an increasingly less absorbed continuum, eventually starting to emit. Another possibility is that the gas is initially accelerated by another mechanism than line driving. One possibility is that the gas is initially dusty, and this dusty gas is accelerated by radiation pressure on the gas due to the radiation field from the accretion disk. Finally, it could be that the low-velocity gas is the origin of the intermediate-ionization lines and is dense enough to be characterized by a lower ionization parameter. Further discussion of these scenarios is left to a future paper.

The final step is to check the consistency of the model. We do this by computing the effective optical depth, t. Then, using this value plus the ionization parameter, U, obtained from the observations, we obtain the force multiplier, $M_L(U, t)$, from the tables given in Arav & Li (1994). This computed force multiplier must be consistent with the value required to accelerate the flow to the observed terminal velocity of 10,000 km s^{-1}. We immediately find that the values of the effective optical depth parameter, t, are on the order of 10^{-7} to 10^{-9}. For $\log U = -0.8$, the tables in Arav & Li (1994) give $\log M_L(U, t)$ of around 3.1. Finally, we consider the fact that we may not be viewing the wind along a streamline, and thus, the velocity that we see is less than the velocity along the streamline by a factor of $\cos \Theta$, where Θ is the angle between the normal and the wind streamline. For each value of $\cos \Theta$, we determine the wind footpoint for the self-consistent solution, defined by the observed ionization parameter, column density, and inferred observed terminal velocity of 10,000 km s^{-1}. An example of the result is shown for two values of $\cos \Theta$ in Figure 11.

If the object is radiating at the Eddington luminosity, the inferred black hole mass is small, so the force multiplier required to accelerate the gas to the terminal velocity is
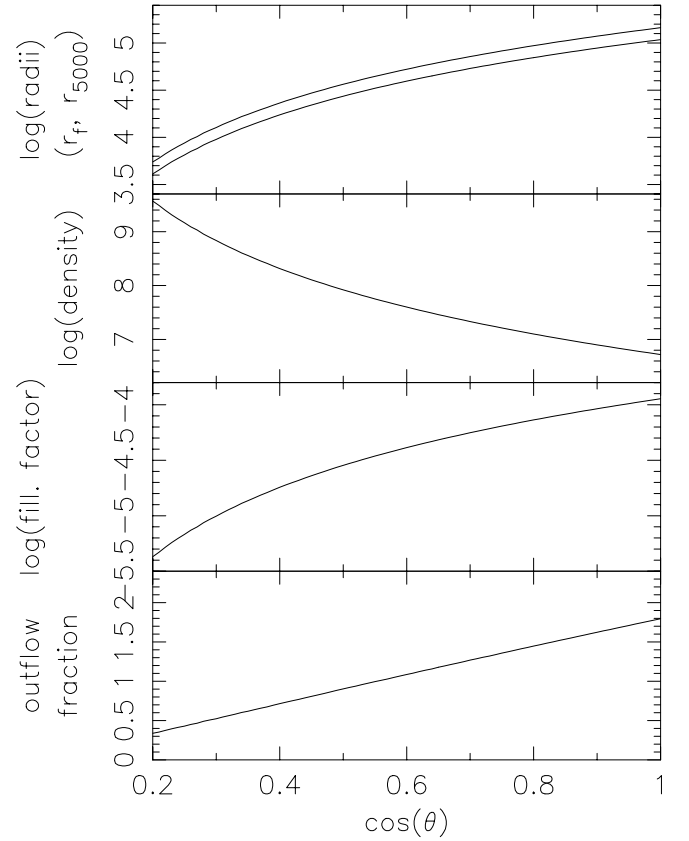
correspondingly small at small values of the footpoint. Thus, the consistency requirement described above is not met for radii smaller than $100,000R_{\rm S}$. This is a very large radius. In contrast, for the larger black hole mass, the force multiplier required to accelerate the gas to a terminal velocity of 10,000 km s^{-1} reaches $\log M_L(U, t) = 3.1$, comfortably between 10,000, and $100,000R_{\rm S}$ for a range of streamline angles with the normal, $\cos \Theta$.

While we cannot rule out a small black hole solely from the kinematics, we do note that this solution is not favored because it implies that the emission region for the wind should be at a larger radius than the emission region for the intermediate-ionization lines, violating our assumption that the wind filters the continuum before it illuminates the intermediate-ionization line-emitting region. Also, these radii are larger than the predicted radius for the breakup of the accretion disk, at which Collin & Huré (2001) propose that some of the line emission is occurring. Hereafter therefore, we discuss only the large black hole mass solution.

In Figure 12, we plot the wind footpoint for the self-consistent solution, defined by the observed ionization parameter, column density, and inferred projected terminal velocity of 10,000 km s^{-1}. We also plot the radius, r_{5000}, at which the projected velocity reaches 5000 km s^{-1}, as well as other physical parameters of the outflow, including density, filling factor, and the fraction of the accretion rate in the outflow,

multiplied by the covering fraction 0.15 obtained by the photo-ionization modeling for the situation in which $L/L_{\rm Edd} = 0.12$, and the X-ray–weak continuum. An approximate measure of the radial extent of the outflow is the difference between r_f and r_{5000} divided by r_{5000}. This parameter is found to be uniformly 0.25. This implies that the wind extends in a fine mist over a fair fraction of the inner tens of thousands of Schwarzschild radii of the AGN.

4. DISCUSSION

4.1. Summary of Inferences from Modeling

The photoionization modeling and toy wind model presented in this paper lead us to draw several conclusions and inferences about the optical and UV emission regions in IRAS 13224–3809 and 1H 0707–495. In these two objects, a continuum that is overall relatively soft and deficient in X-rays illuminates gas with enhanced metallicity. A low column density wind is accelerated that manifests itself through blueshifted high-ionization emission lines including C IV, O IV], Lyα, and N V (the wind component). Representative physical conditions in the wind derived from the photoionization modeling are $\log U = -0.8$, $N_{\rm H} = 10^{21.4}$ cm^{-2}, $n = 10^8$ cm^{-3}, and a covering fraction of 0.15. Using a simple radiative line–driving model and assuming that we see the gas that is accelerated (i.e., no invisible massive substrate is present), we find that the photoionization results are consistent with the dynamical model if the black hole mass is $1.3 \times 10^8\ M_\odot$ and the radius of footpoint of the wind is $\sim$10,000$R_{\rm S}$. We infer that the object is radiating at about 12% of the Eddington limit.

The continuum also illuminates higher density, lower velocity, higher optical depth gas, producing narrow emission lines centered at zero velocity (the disk component). If the continuum illuminates this gas directly, the ionization parameter cannot be higher than $\log U \approx -3$. However, if the continuum passes through the wind before illuminating this gas, the resulting continuum, already weak in the hard X-ray, is now also deficient in extreme UV and the soft X-ray above the helium ionization edge at 54 eV. The result is that the high-ionization lines in the disk component are very weak, if present at all, and thus, the high-ionization lines in the spectrum are dominated by the blueshifted wind components. The disk component is instead dominated by intermediate-ionization lines, including Lyα, Si IV, Al III, Si III, C III], and Fe III. Prominent low-ionization lines, including Mg II, Fe II, and Si II, are also present. The line ratios in the disk component indicate a slightly high density ($\log n = 10.25$), but we note that a shift toward relatively lower ionization lines is expected because of the relatively hard spectrum that the filtered continuum presents (Casebeer & Leighly 2004). If the continuum is filtered through the wind, the inferred ionization parameter is $\log U = -2.1$, and the corresponding radius is 14,000$R_{\rm S}$. A relatively small covering fraction of 0.05 is inferred.

4.1.1. A Few Comments on the Robustness of Results

We note that we do not claim that we can firmly rule out alternative models on the basis of the results presented here. The scenario presented above was chosen because it appears to be most consistent with the data.

We also caution that the models are very simple. Thus, one may be justified in asking, how well do they plausibly conform to the real situation? The ionization model for the wind may be quite generally applicable because we searched a very large region of parameter space: we varied the density, column density, ionization parameter, and covering fraction, as well as the metallicity and continuum shape to some extent. Furthermore, we applied an FOM to quantitatively gauge the applicability of our results. Small improvements will be attained by better constraints on the metallicity that will be possible using the O VI emission (e.g., Hamann et al. 2002) in the FUSE data (K. Leighly et al. 2004, in preparation). The FUSE data will also be very valuable in determining whether there is any variation in ionization with velocity.

How good is the toy wind model? The purpose of the model was to simply make an estimate of the distance to the wind. If radiative line driving is the acceleration mechanism, then the magnitude of the acceleration depends directly on the effective optical depth, which in turn depends directly on the volume-filling factor and the density and inversely on the velocity gradient (Arav & Li 1994). As it is, we obtain the velocity from the conservation of momentum equation. Then, the gradient of the velocity scales with footpoint radius: a wind starting close to the AGN will reach the terminal velocity on a smaller size scale, implying a relatively compact emitting region and large velocity gradient, while a wind starting far from the AGN will reach terminal velocity on a larger size scale, implying a small velocity gradient. The other important constraint comes from the requirement that integrating over the wind yields the same column density as that inferred from the photoionization modeling. Then, combining the size scale with the column density gives the filling factor. Since the integrated column density must be the same no matter where the wind starts, the filling factor and velocity gradient counterbalance each other to make the effective optical depth constant. Thus, the toy model almost boils down to a simple Eddington limit problem; we have determined the radius at which radiation pressure, including radiative line driving appropriate for the ionization state, velocity gradient, and filling factor, that opposes gravity can accelerate the wind to yield the inferred terminal velocity of 10,000/$\cos \Theta$ km s^{-1}.

How could this estimate be refined? A more general velocity law that is frequently used is the so-called beta velocity law, $v(r) = v_\infty (1 - r_f/r)^\beta$, where β is an adjustable parameter that is equal to 0.5 in the case considered above. The velocity gradient for the beta velocity law still scales with the footpoint radius, so if we make the same assumptions as above, that the integrated column is required to be that inferred from the photoionization modeling and that radiative line driving provides the acceleration against gravity, the resulting inferred radius for the emission region would probably not be much different unless extreme values of β were used.

The situation would change if we imagine that there is a significant amount of gas that we do not see that is also being accelerated. For example, as the flow accelerates, some of the gas may become too ionized to emit in the UV; such gas is currently not accounted for. A more massive flow requires a smaller footpoint because a larger radiation force is needed to accelerate it to the terminal velocity. Another potential complication is that the streamlines could change direction, so that the component of the velocity parallel to the line of sight changes. Many other complications could be imagined, and at some point dynamical models, coupled with photoionization models, will be needed.

In summary, the photoionization modeling results appear to be quite general because we searched a large region of parameter space. If we believe that the acceleration mechanism is radiative line driving and that there is no heavy invisible substrate, we may be confident that the radius estimation for

the wind is fairly accurate. It is not possible to put specific confidence limits on the estimate without much more work, which is beyond the scope of this paper.

4.2. Comparison with Previous Results

4.2.1. Wilkes et al. (1999) and Kuraszkiewicz et al. (2000)

Wilkes et al. (1999) investigate emission-line strengths and widths of 41 quasars and compare them with their continuum properties. The quasars are a heterogeneous group chosen because they had *Einstein* spectra; therefore, there is an inherent bias against objects with large values of α_{ox}, as noted in their paper. Also, almost half their sample is composed of radio-loud objects. Among other things, they find an anticorrelation between EW(C IV) and α_{ox}, as we do. In their sample, the objects with the lowest infrared (0.1–0.2 μ) luminosity are five NLS1's and two BALQSOs. These objects all have relatively weak C IV lines; when these objects are removed from the sample, Wilkes et al. recover a Baldwin effect for C IV.

Kuraszkiewicz et al. (2000) follow Wilkes et al. (1999) with a more detailed analysis of the NLS1's in the Wilkes et al. sample, supplementing those with a few additional objects. They analyze some of the same *HST* spectra that we did in Paper I, although they do not look at IRAS 13224−3809 and 1H 0707−495. They include *IUE* spectra as well. They do not attempt a velocity deconvolution of the lines but rather draw inferences from the total flux of the line; certainly, the low resolution of the *IUE* data prevents detailed profile studies. Thus, they perform one-zone CLOUDY modeling of the line flux rather than modeling of two regions, as we do here, although in the end they infer a stratified broad-line region. They infer that a density of 10^{11}–10^{12} cm^{-3} is required to produce the weak C IV and that this density is about 10 times higher than that inferred from reverberation-mapping results (10^{11} cm^{-3}; Peterson et al. 1985). They also infer a low ionization parameter of log $U = -3$.

As noted in § 2.2, our type I solution is quite similar to that inferred by Kuraszkiewicz et al. (2000). Thus, the origin of the differences between our final solution and theirs apparently lies primarily in the much larger region of parameter space that we explored. Also, the velocity deconvolution of the line profile allows us to examine the conditions of the intermediate- and high-ionization line regions separately. Kuraszkiewicz et al. (2000) assume solar abundances; we explore a few cases of enhanced metal abundances. We also use N V, which is very important for constraining abundances and the ionization parameter. Kuraszkiewicz et al. (2000) choose the spectral energy distribution from PG 1211+143, including the infrared. This object appears to have strong X-ray flux and therefore rather powerful heating. As discussed in § 2.2, the abundances and X-ray flux are very important for determining the survival of ions under high radiation fluxes.

4.2.2. Richards et al. (2002)

Richards et al. (2002) recently reported analysis of quasar spectra from the Sloan Digital Sky Survey (SDSS; York et al. 2000). They found that the high-ionization lines, in particular C IV, are systematically blueshifted with respect to the low-ionization lines Mg II and [O III]. They found an anticorrelation between the shift of C IV and its equivalent width, similar to the result reported here. Examination of the profiles of composite spectra constructed according to the C IV blueshift leads them to interpret the shift-EW anticorrelation as a

lack of red wing emission rather than a real shift. This is consistent with the interpretation presented here and in Leighly (2001).

We differ with Richards et al. (2002) on the interpretation of this inference. They propose that all quasars have the same components (e.g., disk, wind, and emission-line regions) and that the anticorrelation is a consequence of differing orientations. Specifically, they propose that blueshifted lines are seen in objects that are edge-on, such as a BALQSO, but that the flow is not directly in the line of sight. The receding red side is blocked by some kind of screen. They find two pieces of supporting evidence for this hypothesis. First, they find similarities in the spectra with the most strongly blueshifted C IV (their composite D) with low-ionization BALQSOs (loBALs). Thus, if all AGNs have BAL winds, and loBALs are viewed at an angle large with respect to the symmetry axis, then composite D objects may be viewed edge-on. However, there is another explanation. Richards et al. (2002) note that both the loBALs and the composite D objects have weak He II. This is classic evidence for weak soft X-ray continuum emission. Thus, it may be that both composite D and the loBALs are soft X-ray−weak, allowing a strong high-ionization wind to form. The second piece of supporting evidence is the fact that there are significantly more radio-detected (FIRST survey) objects in the composite with the least blueshift (composite A) compared with the objects with largest blueshifts (composite D). Since the FIRST survey will resolve out lobe emission, they interpret this as evidence that the composite D objects are edge-on. However, another speculative explanation could be that composite A objects may have radio jets instead of winds and that the base of the jet may provide additional illumination of the disk component, producing stronger emission near the rest wavelength.

A final difference in interpretation comes for the 1400 Å feature for which they note little difference between the composites. The analysis presented here shows that the 1400 Å feature is composed of Si IV from the disk and O IV] from the wind. It may be that the shift of the spectra from disk dominated to wind dominated is accompanied by a shift from Si IV to O IV] in a way that maintains an approximately constant line flux and profile.

4.2.3. Brotherton et al. (1994a, 1994b) and Wills et al. (1993)

In a series of three papers, Wills and Brotherton explored the emission-line properties of a sample of high signal-to-noise ratio rest-frame UV spectra from 123 high-luminosity moderate-redshift AGNs (Wills et al. 1993; Brotherton et al. 1994a, 1994b). They found a number of correlations that are similar to those found here. For example, Wills et al. (1993), in studying the C IV line and the 1400 Å feature, found that as the width of the C IV increased, the equivalent width, kurtosis, and peak-to-continuum intensity decreased. We did not compile the widths of C IV, but we can understand the asymmetry parameter to be nearly equivalent because of our ability to explain the equivalent width−asymmetry anticorrelation observed here as the sum of a strongly blueshifted wind component and a narrow symmetric component (Paper I). They also see the structure of the 1400 Å feature change in a way that can be interpreted as a decrease in the Si IV−to−O IV] ratio with the increasing width of C IV. This seems to be consistent with our idea that when the 1400 Å feature is dominated by disk, corresponding to narrow C IV, it should be primarily composed of Si IV; when dominated by wind, corresponding to

broad C IV, the 1400 Å feature should have a significant component of O IV].

Brotherton et al. (1994b) study the relationship between C IV, the 1900 Å feature composed primarily of C III], and Mg II. They find that as the FWHM of C IV increases, the ratio of C III] to C IV increases. This is consistent with our scenario because when C IV is dominated by wind and therefore is measured to be broad, there is no contribution from the disk to the C IV line, so C III] appears to be relatively strong.

On the basis of these detailed analyses, Brotherton et al. (1994a) propose that the broad lines in active galaxies are composed of two components: a component from an intermediate-line region that consists of a relatively narrow (FWHM ~ 2000 km s^{-1}) line at the systemic redshift and a much broader (FWHM ~ 7000 km s^{-1}), somewhat blue-shifted component. This is similar to our proposed deconvolution. However, the physical interpretation differs. They place the very broad line region very close to the central engine, whereas we place it rather far away from the central engine. Another difference seems to be that they do not consider the possible effect of enhanced abundances or continuum shape. Also, they place the intermediate-line region very far from the central engine, where, as we show, it can be brought into a smaller radius by filtering the continuum through the wind. Interestingly, they derive covering fractions for both regions that are similar to those we do.

4.2.4. *Wills et al. (1999, 2000) and Shang et al. (2003)*

In another series of three papers, Wills and coworkers report the results of analysis of *HST* spectra from a sample of 22 quasars (Wills et al. 1999, 2000; Shang et al. 2003). This sample is drawn from a complete sample of 23 optically selected PG quasars, chosen for their low redshifts and low Galactic hydrogen column densities (see also Laor et al. 1997a).

Wills et al. (1999) present a first look at the spectra and describe an extension of the optical–X-ray Eigenvector 1 to the UV properties. Narrow lines (including C III]) are linked with a larger Si III]–to–C III] ratio, stronger low-ionization lines, weaker C IV, and stronger N V. These are just the properties that describe the spectra of IRAS 13224−3809 and 1H 0707−495. This is not surprising, since these two objects are narrow-line Seyfert 1 galaxies and are sufficiently blue and pointlike to have been classified as PG quasars had they been located in the surveyed portion of the sky, although, like I Zw 1, they would not have been included in the Wills et al. (1999) sample because their Galactic column is too large. Thus, the model that explains our objects can also be applied to the interpretation of the UV extension of Eigenvector 1: C IV is weak because it originates in a wind with little contribution from a narrow symmetric component. N V is strong because abundances are high but also possibly because there is some Lyα pumping of N V in the wind. Low-ionization lines are strong because the continuum is soft and also perhaps because the wind filters the continuum before it illuminates the low-ionization line-emitting region, leaving it no alternative but to cool by low-ionization line emission. Filtering and a soft continuum can also influence the Si III]–to–C III] ratio.

More detailed analysis is presented by Wills et al. (2000) and especially Shang et al. (2003). The UV spectra were combined with optical spectra, and a spectral principal-component analysis was performed over the unprecedentedly large wavelength range. They find that 79% of the variance lies in the first three eigenvectors, but this time the first eigenvector describes cor-

relations between the luminosity and the relatively narrow (FWHM ≈ 2000 km s^{-1}) core of the line. This is interpreted as a manifestation of the Baldwin effect (Baldwin 1977). We discuss the Baldwin effect in the context of our interpretation in § 4.6.2. The second eigenvector found by Shang et al. (2003) is associated with the continuum slope and may be influenced by reddening. The third eigenvector is associated with the traditional first eigenvector discussed by Boroson & Green (1992). It contains all the classic parameters associated with the Boroson & Green (1992) Eigenvector 1 and the UV extension discussed by Wills et al. (1999). An interesting feature is that C IV is very broad in this eigenvector.

4.3. *Other Considerations for the Radius of the High-Ionization Line-emitting Region*

In § 2.2, we showed that the wind emission lines are consistent with three types of photoionization solutions: type I, a high-ionization, high-density solution; type II, an intermediate-ionization, intermediate-density solution; and type III, a solution characterized by a large range of densities. We favor the type III solution because it encompasses a large region of the photoionization parameter space and therefore seems to be the least fine-tuned. But because a large range of densities was allowed by the photoionization solution, the distance from the central engine to the emission region could not be constrained without the toy dynamical model presented in § 2.2. That analysis indicated a radius of $\gtrsim 10,000 R_S$ for a 1.3×10^8 $M_\odot$ black hole, depending somewhat on the angle the flow streamline makes with the observer. In this section, we comment on the consistency of our large radius with reverberation-mapping results, take another look at the type I solution, and investigate the possibility of decreasing the high-ionization line radius for the type III solution by shielding the wind.

4.3.1. *The Type III Solution and Reverberation-mapping Results*

The type III solution combined with the toy dynamical model indicates an emission region for the wind of $\gtrsim 10,000 R_S$ for a mass of 1.3×10^8 $M_\odot$, depending somewhat on the angle the flow streamline makes with the observer. This corresponds to a distance of 3.8×10^{17} cm, or about 150 lt-days. On the face of it, an origin of the high-ionization line-emitting wind at such a large radius seems to be in conflict with reverberation-mapping results, which find evidence for an ionization-stratified broad-line region in which high-ionization lines are produced quite close to the central engine. For example, in NGC 5548, an object with UV luminosity 4 times smaller than that of IRAS 13224−3809 and 1H 0707−495, the lag of the high-ionization lines behind the continuum is on the order of 1 week or less (Korista et al. 1995). In fact, there may be no conflict. As discussed in Paper I, the high-ionization lines in NLS1's can be considered to be composed of two components: the broad blueshifted component that is produced by the wind and the narrow symmetric component that is associated with the disk. Reverberation-mapping results are probably dominated by the narrow symmetric core that should be produced at smaller radii. Observations support this hypothesis, since in some cases the cores of the lines vary more than the wings (e.g., Wandel et al. 1999). This can be considered to be evidence that the broad component is produced by optically thin gas, which is less responsive to continuum changes (Shields et al. 1995). However, it could also be produced if the wind is physically far from the central engine, as is inferred here.

4.3.2. The Type I Solution Reconsidered

In this section, we take another brief look at the type I solution. As discussed in § 2.2, in this solution the density is constrained to very high values, $\log n \gtrsim 11.5$. The high-density results in partial thermalization of Lyα and C IV relative to Si IV; thus, the observed low equivalent width of C IV is explained. This solution is quite similar to the result obtained by Kuraszkiewicz et al. (2000), who analyzed UV spectra of NLS1's but considered only the integrated line fluxes and did not analyze the line profile. The high density and high inferred ionization parameter ($\log U = -0.4$) imply a high photon flux ($\log \Phi = 22.5$), which then implies that the emission region is located quite close to the central engine at $R = 6.1 \times 10^{15}$ cm for $H_0 = 50$ km s^{-1} Mpc^{-1} and $q_0 = 0.5$ (our default choice of cosmological parameters), or 2.7×10^{15} cm for $H_0 = 70$ km s^{-1} Mpc^{-1}, $\Omega_M = 0.3$, and $\Lambda_0 = 0.7$. A radius of 6.1×10^{15} cm corresponds to $160 R_S$ for our larger black hole mass of $1.3 \times 10^8 M_\odot$. This value is somewhat smaller but has the same order as the inferred location of the disk wind proposed by Murray et al. (1995) of $600 R_S$.

It would be easy to differentiate between type I and III solutions from the variability of the high-ionization lines. First, the inferred radius for the type I solution implies a light-travel time from the central engine to the emission region of 1–2.4 days; thus, the emission lines could respond rapidly to changes in the continuum. For the type III solutions, no variability would be expected on short timescales because the light-travel time is large. Furthermore, the type I and type III solutions are characterized by different column densities and different continuum opacities. Both are optically thin to the continuum; however, the type III solution is thinner, so that while the highest ionization lines, O VI and N V, should vary in response to the continuum, since they are produced in front of the helium ionization front, C IV is produced deeper in the photoionized slab, so it should saturate in response to flux changes (e.g, Shields et al. 1995). For the type I solution, O VI, N V, and C IV are all produced near the illuminated face of the cloud, implying that they would all vary in response to the continuum. Finally, the dynamical timescale for the type I solution, assuming a $1.3 \times 10^8 M_\odot$ black hole, is less than a year, so one might expect to see changes in the line profile also.

There may be an additional problem with the type I solution. When the densities are so high that the lines are thermalized, the cooling is dominated by continuum emission, such as the Balmer continuum (Rees et al. 1989). Neither IRAS 13224$-$3809 nor 1H 0707$-$495 shows an especially strong Balmer jump (note that the Balmer jump can be distinguished from the strong Fe II by the wavelength of onset; e.g., Dietrich et al. 2002).

4.3.3. Can Murray et al. Shielding Reduce the Radius of the High-Ionization Line-emitting Region?

In 1995, Murray et al. suggested that a wind driven by resonance scattering could have a relatively small footpoint ($\sim 600 R_S$) if there is also present a region of highly ionized gas ($U = 10$) that shields[8] the wind from the strongly ionizing soft X-ray emission from the central engine. They then suggest that this wind could emit broad emission lines under the condition that $U = 1$–10. Recalling that our best estimated ionization parameter for the type III solution is $\log U = -0.8$, this implies that this shielding would allow the wind emission to be produced where fluxes are 100–1000 times higher, corresponding to radii more than 10 times smaller, assuming the same density. However, on the basis of our experience with "filtering" as applied to the disk emission lines, we suspect that this scenario is untenable because there would not be sufficient high-energy photons in the shielded continuum to create and excite the highly ionized ions that we see in the wind. In this section, we numerically test the effect of shielding on the emission from the wind.

We devised the following numerical experiment. We transmitted our hard low-flux continuum through shielding gas having a metal abundance and a nitrogen abundance a factor of 5 and 10 over solar, respectively, and then used that transmitted continuum to illuminate the wind. The parameters describing the shielding gas are as follows: we uniformly use $U = 10$ and consider a range of column density from 10^{21} to $10^{22.8}$ cm^{-2}. The parameters describing the wind are the following: it has a uniform $N_H^{max} = 22$ and a range of ionization parameters from $\log U = -1$ to 0.5. Note that, as before, since we are interested in obtaining the radius of the emission region, the U-values that we quote are appropriate for the unabsorbed continuum.

We determine a reference point for the simulations as follows. The transmitted continuum will be almost identical to the incident continuum for the extreme minimum of shielding column density of 10^{21} cm^{-2}, because for $U = 10$ that gas will be almost completely ionized. Then, since the adopted value of $N_H^{max} = 22$ and extreme minimum value of $\log U = -1$ for the wind are close to the best wind parameters derived in § 2.2, the results of this combination of parameters will be close to the observed values. Therefore, we adopt the results from this extreme combination of parameters as reference values with which to compare the results for larger values of shielding N_H and larger values of wind ionization parameter $\log U$. The reference points lie in the bottom left corner of each panel in Figure 13.

We plot contours of the normalized equivalent width, defined as the predicted equivalent width divided by the equivalent width obtained for the reference set of parameters described above; thus, contours marked "1.0" terminate necessarily in the lower left corner of each plot. These contours show that as the shielding column density increases from left to right across each plot, the highest ionization lines decrease, as the photons required to create the emitting ions are removed from the continuum. At the same time, the gas is still subject to an intense photoionizing continuum, and it responds by increasing emission of lower ionization lines. As the radius decreases, the line emission decreases as ions become overionized.

We interpret these results in terms of the Murray et al. (1995) and Murray & Chiang (1998) scenarios as follows: shielding by highly ionized gas can certainly increase the emission of intermediate- and low-ionization lines at higher fluxes than would be possible without shielding. However, shielding does not affect high-ionization lines in the same way, because the photons absorbed by the highly ionized gas are those required to create ions such as N^{+4} (ionization potential 77 eV) and O^{+5} (ionization potential 113 eV). Therefore, we conclude that shielding cannot bring the wind closer to the

---

[8] As discussed in § 2.3, we differentiate between a shielded continuum, which is assumed to have been transmitted through highly ionized gas (e.g., Murray et al. 1995), and a "filtered" continuum, which is assumed to have been transmitted through the wind while ionizing and exciting it before illuminating the disk and producing the observed intermediate- and low-ionization lines.
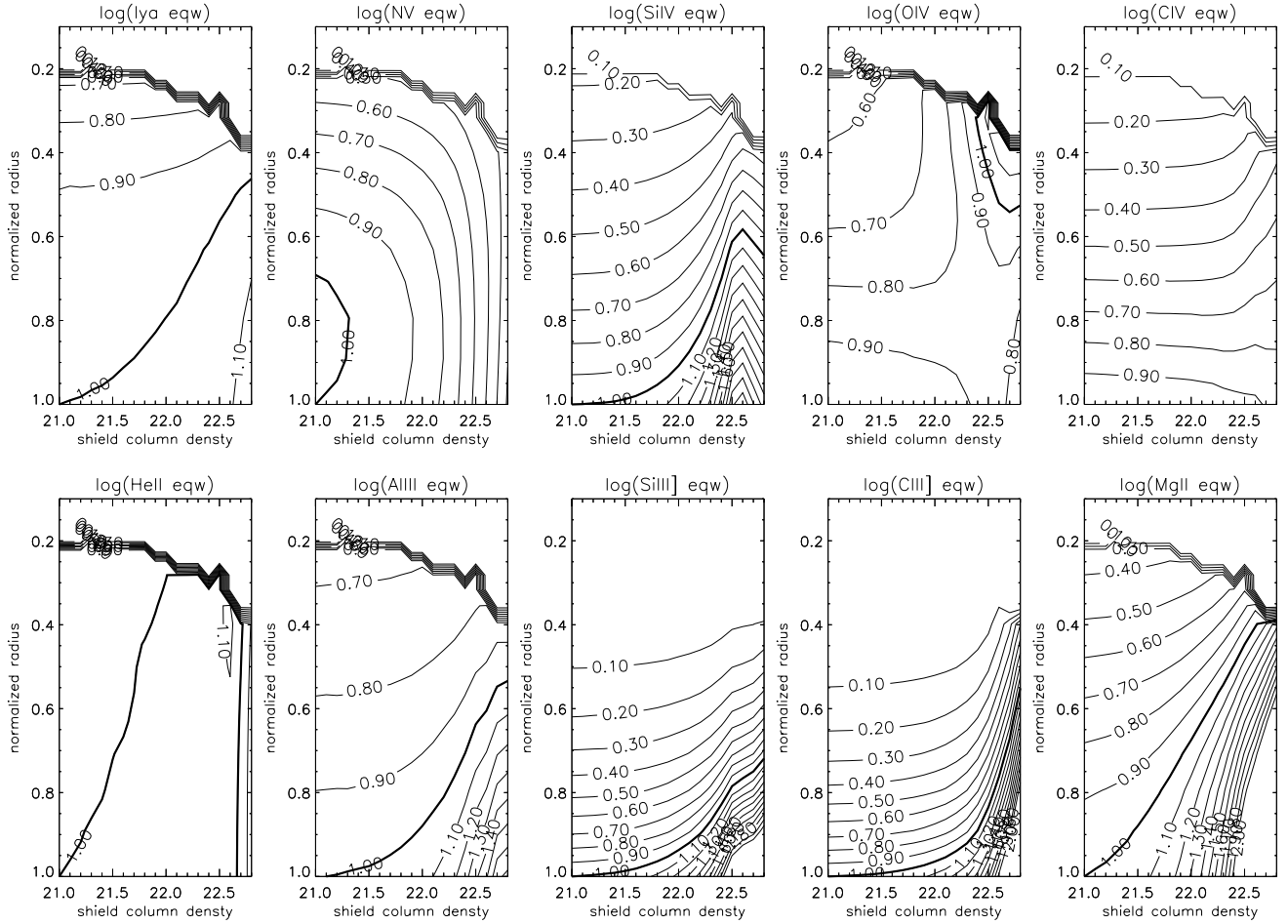
Fig. 13.—Test of the effect of shielding, with contours of normalized equivalent width, constructed with a covering fraction of 0.2. Normalization has been done with respect to the nominal solution at the lower left corner of each plot; this is nearly equivalent to the solution obtained in § 2.2. The x-axis shows the column density of the shielding gas, which has the ionization parameter $U = 10$. The y-axis plots the radius with respect to the nominal value in the lower left corner of each plot. The thick contour intersecting the lower left corner of each plot shows the nominal value for each emission line. See text for further details.

nucleus. We note that this conclusion is not dependent on the column density in the wind. We examined higher column densities and found that while the flux in other lines increased, the N v line contours stayed the same, which means, not surprisingly, that with $N_H^{max} = 10^{22}$ cm^{-2} we integrate through the entire N^{+4} zone.

4.4. Constraints on the Intermediate-Ionization Lines

In Paper I, we discovered several correlations among the equivalent widths and ratios of the intermediate-ionization lines C III], Si III], and Al III in our sample of NLS1's. Specifically, we find that both the C III]/C IV and the Si III]/C III] ratios are correlated with Si III] and Al III equivalent widths but are anticorrelated with the C III] equivalent width. As discussed in Paper 1, these correlations could originate in a variation in density, ionization parameter, or continuum shape.

To investigate quantitatively the complex interdependencies of these three parameters, we run some CLOUDY models using the hard low-flux continuum. We examine the equivalent widths of C IV, Al III, Si III], and C III] as a function of density for a constant covering fraction of 0.05 and two ionization parameters (log $U = -2$ and -3). We assume that the gas is ionization bounded. We compute the equivalent widths under two assumptions: that the continuum illuminates the

emitting gas directly and that the continuum illuminates the gas after passing through the wind, as discussed in § 2.3. The results are displayed in Figure 14.

Figure 14 shows the decrease in equivalent width as a function of density expected for the semiforbidden lines C III] and Si III]. The permitted line C IV shows little dependence on density, while Al III shows a moderate increase, possibly because of its increasing role in cooling in the C III]– and Si III]– forming region. This seems to suggest that if an increase in density drives the correlations, the C III]–to–C IV ratio should decrease, contrary to the observations.

Filtering the continuum through the wind results in a dramatic decrease in C IV. In fact, the decrease is larger between the filtered and nonfiltered continua when log $U = -2$ than the decrease between log $U = -2$ and -3 for either of the two continua. For log $U = -2$, there is little effect on the intermediate-ionization lines Al III, Si III], and C III], although we see a slight increase for Si III] for the filtered continuum. For log $U = -3$ and a filtered continuum, all the lines become weaker, with C IV weakening the most.

These simple simulations show that the origin of the correlations among the intermediate-ionization line properties could be a filtered continuum or it could originate from a trend in ionization parameter, but an origin in density variation does not seem to be supported.
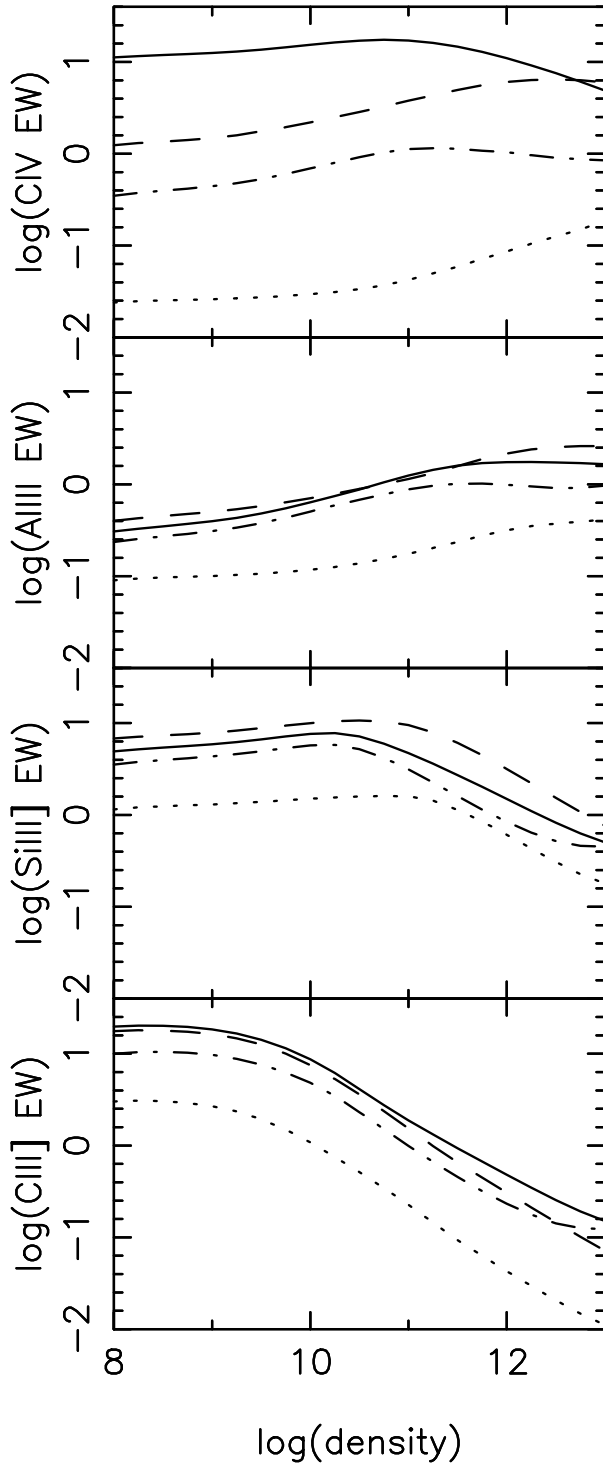
those two objects compared with a heterogeneous sample of NLS1's. In this section, we attempt to use these results to construct a scenario for the emission regions in NLS1's.

Perhaps the simplest scenario for the emission-line geometry consists of an accretion disk with a wind. The blueshifted part of the lines is produced in the wind, while the portion centered at the rest wavelength is produced in the base of the wind or in the accretion disk itself. In some objects, there is no significant wind, in which case all the line emission comes from the base of the wind. In others, the wind emission is relatively strong; in these objects, high-ionization lines have a blue wing arising from the wind.

Why do some objects have winds and others do not? If the winds are accelerated by radiation line driving, then objects with steep α_{ox} may have winds, while objects with flat α_{ox} may not. This is because a strong UV continuum is necessary to drive the wind; however, too much soft X-ray emission will easily overionize the gas, destroying the resonance-scattering ions. A high metallicity may also encourage a wind, since that could contribute more resonance-scattering ions.

This is the simplest scenario; however, it does not explain a number of aspects of the data. It does not explain why C IV is so weak in the wind-dominated NLS1's such as IRAS 13224−3809 and 1H 0707−495; the scenario above allows only blue wings, and the C IV line core and other high-ionization line cores produced in the base of the wind should still be very strong and should dominate the line emission. It also does not explain the extreme line ratios in the wind-dominated NLS1's, including relatively large C III]/C IV, Si III]/C III], and Al III/C III] ratios. Additional tweaks of the scenario are necessary to explain these properties.

How to explain the weak C IV core in the wind-dominated NLS1's? Increasing the density will not help. Although the high Si III]/C III] ratio suggests a higher density in these objects, the inferred density, well constrained by the Si III]/C III] to be $\log n \approx 10.25$, is not nearly high enough to suppress C IV, a permitted line. This point was discussed in detail in § 4.4.

Another possibility is to simply move the emission region very far from the nucleus such that the dominant ionization state for carbon in the base of the wind is C^{+2}. This possibility is explored in the context of photoionization modeling in § 2.3. There are two potential objections to this. First, the inferred distance to the emission region is very large, so that for reasonable black hole masses, the Keplerian velocities are quite low. A more important problem would be, Why is the emission region exceptionally far from the nucleus in the wind-dominated NLS1's alone? One possible answer could be to associate the emission region with the breakup radius of the accretion disk (Collin & Huré 2001), as that should vary with accretion rate (Huré 2000). However, this does not simply solve the problem, since the breakup radius depends inversely on accretion rate; the larger the accretion rate with respect to the Eddington rate, the smaller the radius, just the opposite dependence required if we associate the wind-dominated NLS1's with a higher accretion rate.

In § 2.3 we present a scenario that explains these observational results naturally. If the continuum is transmitted through the wind before it illuminates the intermediate- and low-ionization line-emitting gas, it will lack sufficient photons in the helium continuum to excite high-ionization lines. Thus, the presence of a wind naturally results in a weak core for the high-ionization lines. The softening of the continuum also tends to create and excite ions with lower ionization potentials;
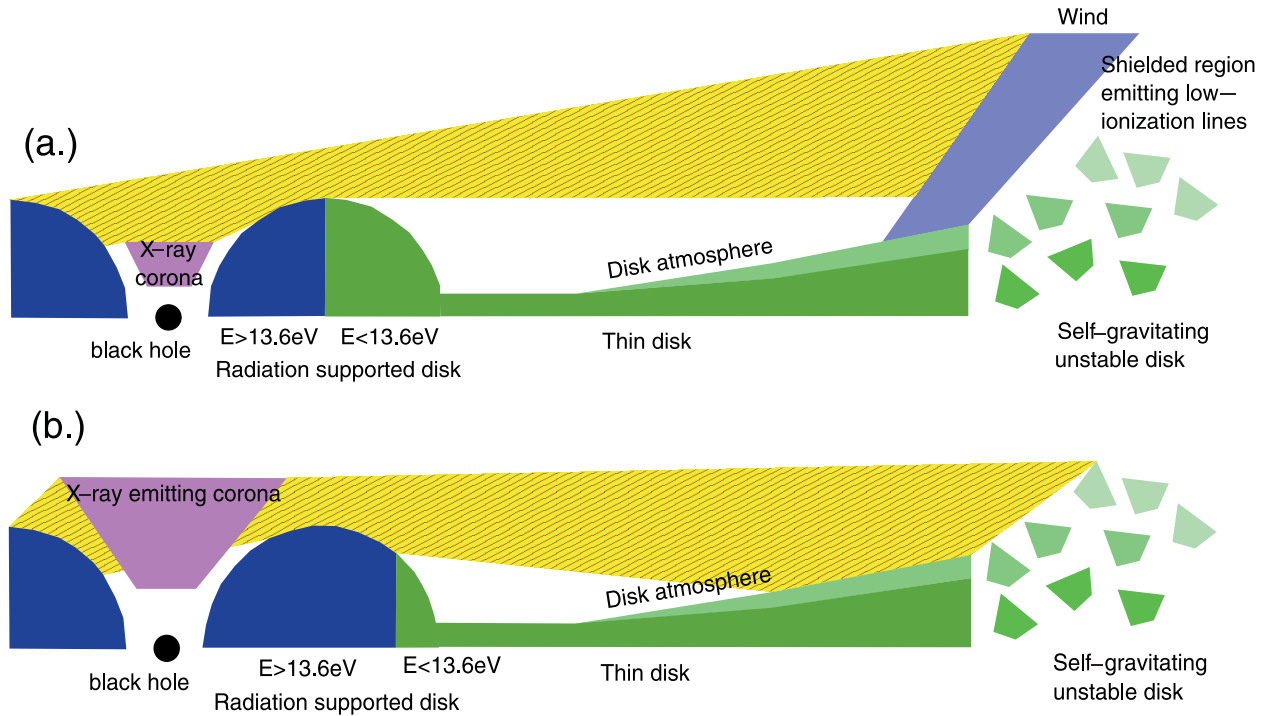

Fig. 14.—Mutual influence of density, spectral shape, and ionization parameter for C IV, Al III, Si III], and C III]. The hard low-flux continuum is assumed, and the assumed covering fraction is 0.05. For each emission line, the solid line denotes $\log U = -2$ and direct illumination, the dashed line denotes $\log U = -3$ and direct illumination, the dash-dotted line denotes $\log U = -2$ and a filtered continuum, and the dotted line denotes $\log U = -3$ and a filtered continuum.

4.5. Ideas and Speculations about the Emission Regions in NLS1's

In this paper and in Paper I, we learned many things about the UV emission lines from two particular NLS1's, 1H 0707−495 and IRAS 13224−3809, and about the properties of

Fɪɢ. 15.—Schematic diagram referenced in § 4.5.1 (not to scale). Red diagonal lines with yellow background show rays of photoionizing light. (*a*) Geometry that encourages a wind to develop. The wind then shields the intermediate- and low-ionization region possibly associated with the self-gravitating, unstable disk (Collin & Huré 2001). The outside of the radiation-supported disk emits primarily light that initially accelerates but does not overionize the wind. (*b*) Geometry that does not produce a wind. A significant amount of photoionizing light is emitted by the outside of the radiation-supported disk. This overionizes the tenuous part of the disk atmosphere, preventing a wind from forming. The disk atmosphere is illuminated by photoionizing light, causing high-ionization lines to form that will be symmetric and centered at the rest wavelength.

this can partially explain the dominance of Si III] and Al III in the intermediate-ionization line-emitting region.

4.5.1. *A Speculative Scenario*

The analysis presented in this paper and in Paper I leads us to infer that the spectral energy distribution is a primary factor in determining both the ionization and the dynamics of the line-emitting gas in AGNs. A continuum strong in the UV and weak in the X-ray can drive a wind by resonance scattering without overionizing the ions required for the line driving; this results in blueshifted high-ionization lines. This wind may then filter the continuum before it illuminates lower velocity gas-emitting intermediate- and low-ionization lines. The filtered continuum lacks high-energy photons, so the low-velocity gas cools by emitting particularly lower ionization lines, including such low-ionization lines as Fe II and Si II. Conversely, if the X-rays are strong compared with the UV, a wind is not formed because the gas is overionized before it can be accelerated. This un-filtered continuum illuminates the lower velocity gas directly without being filtered. This continuum is strong in the extreme UV and in the X-ray, so higher ionization lines, including C IV, are produced in the low-velocity gas.

The scenario outlined above begs the question, What determines the continuum to begin with? The continuum may be directly controlled by intrinsic parameters such as the black hole mass and accretion rate, but how? We present a specula-tive scenario to explain this as follows. Under conditions of moderate accretion rate, the accretion disk may be "thin," at least at large radii (e.g., Frank et al. 1992). The thin disk is able to radiate the power that it generates and is optically thick and geometrically thin. Its spectrum is predicted to be $F(\nu) \propto \nu^{1/3}$. Increasing the accretion rate causes the characteristic temper-

ature to increase; increasing the black hole mass causes the characteristic temperature to decrease (e.g., Ross et al. 1992). Thus, the thin disk can produce a blue continuum in the optical and UV that is harder for smaller black hole masses and higher accretion rates.

At smaller radii, the thin disk is predicted to generate more energy than can be radiated through its surface. Radiation pressure should become important, causing the disk to puff up and become geometrically thick. The simplest radiation pressure–dominated disks are known to be unstable; however, detailed models show that this solution still may be viable (e.g., Agol et al. 2001; Blaes & Socrates 2001).

X-rays are thought to be produced close to the black hole by an optically thin, hot corona that intercepts optical/UV pho-tons and upscatters them. The amount of X-ray emission depends on the amount of corona, specifically on the covering fraction and optical depth. The amount of corona may depend on how much accretion energy is diverted into producing the corona, for example, by magnetic reconnection of buoyant loops generated in the disk that escape through the surface. Some recent models predict that the amount of energy pro-duced in the corona should also depend on the accretion rate (e.g., Liu et al. 2002), so that high accretion rate objects have a smaller fraction of energy emitted in the corona compared with the disk. This scenario was used by Bechtold et al. (2003) to explain the steepening of $\alpha_{\rm ox}$ with luminosity.

So, combining the thin disk, the radiation-supported thick disk, and the corona, we suggest the speculative geometric scenario illustrated in Figure 15 (not to scale). The key feature that could explain the behavior of the UV emission lines in NLS1's is the spectrum emitted by the outer part of the geo-metrically thick disk, because that is the spectrum that initially

illuminates the line-emitting gas. If that continuum is dominated by photons below 13.6 eV, it can accelerate a wind without overionizing it. That accelerated wind, which may originate in the region where the disk becomes gravitationally unstable, reaches a modest velocity yet does not emit very much line emission. As it rises above the lip of the radiation pressure–supported torus, it is exposed to the full UV continuum, is quickly accelerated, and emits. An analogy may be wind blowing snow off a cornice. Beyond the wind may lie the clumps from the gravitationally unstable disk that would emit the lower velocity intermediate- and low-ionization lines when they are illuminated by the continuum filtered through the wind.

In contrast, if the spectrum of the outer part of the geometrically thick disk emits very much radiation at energies above 13.6 eV, the potential reservoir for the wind gas is exposed to the full ionizing continuum and is overionized before it can be accelerated. Furthermore, the thin disk will be illuminated by a strong photoionizing continuum, and it will cool by emitting strong permitted lines including C IV.

This speculative scenario explains the emission lines, but it can also explain the continuum. Quasars that have strong blueshifted lines tend to have blue optical and UV continua. This may be a consequence of the optical/UV emission from the thin disk dominating to a small radius. An example of such an object is PHL 1811, a very luminous quasar (K. Leighly et al. 2004, in preparation) Conversely, objects that do not have blueshifted high-ionization lines may have less contribution from the optically thick, geometrically thin disk; their continuum is stronger in the extreme UV and may peak in the soft X-ray. An example of such an object is RE 1034+39 (Casebeer & Leighly 2004).

4.6. Other Considerations

4.6.1. Influence of X-Ray Properties

We have noted already that IRAS 13224−3809 and 1H 0707−495 have extreme X-ray properties compared with other NLS1's, as discussed by Leighly (1999b). These properties include the highest amplitude X-ray variability and the most prominent X-ray–soft excesses in their *ASCA* spectra. As discussed above, the photoionization modeling shows that a larger region of parameter space is available when the X-ray flux is low. We justified our assumption of low X-ray flux using the fact that 1H 0707−495 has been frequently found in very low flux states, a factor of 10 lower than observed when the *ASCA* spectrum was made (Leighly et al. 2002; K. Leighly et al. 2004, in preparation). Furthermore, in Paper I, we showed that there is an anticorrelation between the asymmetry of the emission line and $\alpha_{\rm ox}$, such that X-ray–weak objects have blueshifted profiles.

It is also possible that the high-amplitude variability plays a role in the production of the emission lines. If the high-amplitude variability extends from the X-ray into the UV, a variable radiation line–driving force or a variable photoionizing continuum may be present. A variable line-driving force may be interesting because it could produce shocks in the wind that may result in density enhancements and may help formation of filaments dense enough to emit the lines that we see. A variable photoionizing continuum can affect the ionization balance of the emitting region; Nicastro et al. (1999) found that the effect was such that the emission region was overionized compared with the ionization expected for that particular ionization parameter.

There are no data yet that support rapidly variable UV emission in these two objects. Young et al. (1999) do not see any optical variability on short timescales over three nights in IRAS 13224−3809. No significant variability in the near-UV was detected during a 20,000 s *XMM-Newton* Optical Monitor observation. However, observed correlated optical and X-ray variability in NGC 5548 led Uttley et al. (2003) to propose that relatively luminous Seyfert galaxies may be more variable in the UV than less luminous objects because of the relatively cooler accretion disk expected for a larger black hole and the corresponding shift of the UV emission region to smaller $R/R_{\rm S}$, for which dynamical timescales may be short. Thus, variability in the line-driving continuum or photoionization continuum may be possible.

4.6.2. The Baldwin Effect

It is well known that the equivalent widths of emission lines in quasars are anticorrelated with their luminosity (the Baldwin effect; Baldwin 1977; see Osmer & Shields 1999 for a review). The Baldwin effect has been attributed to variations in the broad-line cloud-covering fraction, ionization parameter, and inclination. Perhaps the most promising explanation is the one in terms of the shape of the continuum because it can explain the fact that the higher ionization lines experience a steeper decrease with luminosity than the lower ionization lines. Another interesting feature of the Baldwin effect is that it is stronger in the line cores. This fact was also observed in the spectral PCA analysis of the *HST* sample of PG quasars (Shang et al. 2003).

It is possible that our scenario can contribute to the interpretation of the Baldwin effect. Luminosity may be correlated with the black hole mass, thus predicting a softer spectrum for larger black holes for a fixed accretion rate relative to the Eddington rate (e.g., Ross et al. 1992). Thus, more luminous objects, because of their softer spectrum, may produce a wind that may filter the continuum, reducing the availability of energetic ionizing photons to the low-velocity gas and reducing the line core. Interestingly, Shang et al. (2003) find that broad He II $\lambda 4686$ is present in their first eigenvector, which they interpret as having an origin in the Baldwin effect, and is correlated with the strength of the narrow component of the lines. As discussed above, He II is the classic indicator of a continuum strong in the soft X-ray. It is also interesting to note that this interpretation contrasts with that of Shields et al. (1995); they speculate that the covering fraction of the optically thin component depends inversely on luminosity.

4.6.3. BALQSOs

In this paper, we show that a number of the emission-line properties of NLS1's are plausibly related to the presence or absence of a radiatively driven wind. The other class of active galaxies for which there is good evidence for a radiatively driven wind is the BALQSOs. Of course, there is an important difference between BALQSOs and NLS1's: in BALQSOs the wind is in the line of sight to the nucleus, causing sometimes spectacular absorption lines to be imprinted on the spectrum, while in NLS1's the wind is not in the line of sight. This difference could be simply a matter of orientation. One sees emission lines regardless of the viewer orientation (disregarding anisotropic emission for the moment), so if the wind has some effect on the emission-line properties of NLS1's, then it may produce the same effect on the emission lines in BALQSOs.

Weymann et al. (1991) present a comprehensive comparison between the emission-line properties of BALQSOs and non-BAL quasars. As discussed in the introduction to that paper, their work was motivated by reports of the following differences between BALQSOs and ordinary quasars: (1) Fe II is stronger; (2) Al III is stronger; (3) C IV is weaker; and (4) N V is stronger. We note that these properties describe the differences between NLS1's and ordinary broad-line quasars. Weymann et al. (1991) then present a very careful and conservative analysis of samples of BALQSOs and non-BALQSOs. While they conclude that, excluding the loBALs,[9] the emission lines are very much the same in BALQSOs and non-BALQSOs, a few subtle differences remain. There is an enhancement of N V, and there is an enhancement around Al III, which they attribute to Fe II or Fe III. They also find a correlation between Fe II and "the balnicity" index, a measure of the BAL-ness of a quasar. In our scenario, these properties would be explained as follows. The N V enhancement arises in the BAL flow, and it is perhaps enhanced by scattering (as noted by Weymann et al. 1991). However, we also speculate that the strong low-ionization lines result from illumination by a continuum filtered through the BAL flow. We point out that in our scenario, in general the lines such as C IV are composed of both wind and disk components, and thus, differences between objects with and without winds may not be very spectacular.

If the radiatively driven winds in BALQSOs are related to the winds that we discuss in this paper, we might also expect that BALQSOs should be deficient in X-ray emission. Measuring the X-ray emission from BALQSOs is difficult because the X-rays are usually absorbed, and it is difficult to deconvolve the spectrum and the absorption robustly without making assumptions about the continuum shape. Sometimes, good evidence for normal spectral energy distributions was found (e.g., Gallagher et al. 2002). However, there is at least one instance in which evidence that the BALQSO is intrinsically X-ray–weak was found (Sabra & Hamann 2001).

4.6.4. Early Universe Counterparts of NLS1's

Recently, several investigators have sought the early universe counterparts of NLS1's (e.g., Mathur 2000). This is important because now a significant number of quasars with redshifts $z > 4$ have been discovered. This epoch corresponds to more than 90% of the age of the universe; therefore, these quasars are young. The accretion rate in these objects is of special interest. Luminous quasars must have large black holes, and to grow large in such a short time, they ought to be accreting at a rapid rate.

The properties of the objects discussed in this paper may give us a hint about what kind of objects at high redshift correspond to narrow-line Seyfert 1 galaxies. Some objects have been found that have extremely strong and narrow emission lines (e.g., Constantin et al. 2002). The lines in these objects have huge equivalent widths; clearly, the emitting region is very well illuminated. If we consider the fact that the Baldwin effect slopes for NLS1's typically lie significantly below that of other quasars (Paper I; Wilkes et al. 1999), then that argues against these high equivalent-width objects being early universe counterparts of NLS1's.

On the other hand, several high-redshift objects have been discovered in the SDSS that have very blue continua and no

apparent emission lines (Fan et al. 1999; Anderson et al. 2001). One of the properties of NLS1's is their relatively low line equivalent width and frequently blue continua. Thus, the line-less quasars seem much more similar to the high-luminosity NLS1's, and therefore, they may be the sought-after early universe counterparts (Leighly et al. 2004; K. Leighly et al. 2004, in preparation).

5. SUMMARY

1. This is the second in a series of two papers devoted to understanding UV line emission in NLS1's. In the first paper (Leighly & Moore 2004), we present the results of analysis of *HST* STIS spectra of the extreme NLS1's IRAS 13224−3809 and 1H 0707−495. Those spectra reveal broad blueshifted high-ionization emission lines, and intermediate- and low-ionization lines that are narrow and centered at the rest wavelength. We interpreted this as evidence that the high-ionization lines are emitted in a wind and that the intermediate- and low-ionization lines are emitted in the accretion disk or base of the wind. We developed a template profile for the wind from the C IV line, then modeled the strongest lines in the spectra using the wind template and a narrow symmetric component. We found that the following lines are dominated by wind emission: C IV, He II, and N V. These lines are dominated by disk emission: Al III, Si III], C III], and Mg II. Lyα and the 1400 Å feature composed of Si IV and O IV] have both disk and wind components.

2. The photoionization code CLOUDY was used with the results of Paper I to determine the conditions of the line-emitting gas. For the wind, we investigated the effects of a large range of density, photoionizing flux, a parameter related to column density ($\log N_H^{max} = \log N_H - \log U$), the covering fraction, and a few combinations of metallicity and continuum shape. We compared the simulation results with the data, using a figure of merit defined to be the absolute value of the difference between the logarithm of the simulated and that of the observed equivalent widths. We found evidence for three minima in parameter space. The type I solution, obtained for every combination of metallicity and continuum, was characterized by a very high density ($\log n \geq 11.5$,) high ionization parameter ($\log U \geq -0.6$), and large column density ($\log N_H^{max} \geq 23$). This is similar to the result obtained by Kuraszkiewicz et al. (2000) for NLS1's without profile deconvolution. When the metallicity was enhanced and the continuum was X-ray–weak, the type III solution, characterized by a large range in density ($-7 < \log n < 11$), high ionization parameter ($-1.2 < \log U < -0.2$), and a low column density ($\log N_H^{max} \approx 22.2$), was obtained. A much larger region of parameter space is encompassed by the type III solution; therefore, it appeared to be less fine tuned and more physically realistic than the type I solution.

3. Photoionization modeling for the disk lines was performed using the results from the photoionization modeling of the wind lines. That is, metallicity was assumed enhanced, and an X-ray–weak continuum was used. The ratio of the intercombination lines Si III] and C III] provided a good density constraint ($10 < \log n < 10.5$). The low limit on a disk contribution of C IV and a corresponding low ratio of C IV to C III] require a low value of the photoionizing flux ($\Phi = 17.5$) and a very large radius for the emission region (1.9×10^{18} cm). However, if the continuum is "filtered," or transmitted through the wind before it illuminates the intermediate- and low-ionization line-emitting region, the photoionizing flux can be higher ($\Phi = 18.7$) and the emission region radius smaller

---

[9] Other authors have remarked on the similarity between NLS1's and the loBALs, objects that have very strong Fe III and Fe II lines (e.g., Leighly et al. 1997; Boroson & Meyers 1992 for the case of I Zw 1).

$(5.3 \times 10^{17}$ cm). The difference is that the filtered continuum lacks photons in the helium continuum, so it is not able to produce C IV as efficiently. Such a filtered continuum naturally produces the strong lower ionization lines seen in NLS1's.

4. We used the photoionization results to infer the location of the emission regions. We used two candidate black hole masses: a small one, obtained assuming that the object was radiating at the Eddington limit, and a larger one ($1.3 \times 10^8 M_\odot$; $L = 0.12 L_{\rm Edd}$), obtained directly from the photoionization modeling results for the intermediate-ionization emission lines. We assumed the type III wind solution, which by itself provides little constraint on density and therefore no constraint on radius. To obtain a radius constraint for the wind, we used a simple dynamical model in which the wind is accelerated by radiative line driving. We find that the larger black hole mass is better accommodated by the dynamical model results. Representative values of the parameters inferred for the wind are a density of $\sim 10^{8.5}$ cm^{-3}, a radius of $\sim 10^4 R_{\rm S}$, a filling fraction of $\sim 10^{-5}$, and a wind outflow rate about half that accreted into the black hole.

5. We discuss the results of both papers and compare with previously published results. The discovery, presented in Paper I, that blueshifted line profiles are associated with steep $\alpha_{\rm ox}$ seems to provide evidence for radiative line driving as the wind acceleration mechanism. The concept of filtering the continuum through the wind before it illuminates the intermediate- and low-ionization line-emitting gas may help explain the very strong low-ionization line emission seen in many NLS1's and some other windy objects such as BALQSOs. We also provide a speculative scenario that may explain the range of UV emission-line properties in NLS1's.

APPENDIX

FURTHER COMMENTS ON THE BLACK HOLE MASS AND ACCRETION RATE

In § 3, we make two estimates of the black hole mass. The first assumed the luminosity to be Eddington, simply because the Eddington luminosity is a fiducial parameter of the system. This estimate was not favored because it predicted a velocity too low for the C III]–emitting region (§ 3.1) and because the mass was so low compared with the luminosity that the force multiplier required to accelerate the wind to the observed terminal velocity was lower than that implied by the gas properties (§ 3.2). The second estimate was made on the basis of the calibration of the photoionization and reverberation techniques described by Wandel et al. (1999), although we did not make precisely the same assumptions as they did (see below). The second estimate could indeed explain the width of the C III] line, not surprisingly, since that is built into the assumptions used in the calculation. Also, we could get a reasonable match between the force multiplier required to accelerate the gas to the terminal velocity and the force multiplier defined by the gas properties. We then infer that the object is radiating at 12% of the Eddington luminosity and that the photoionizing continuum is 8% of the Eddington luminosity. This is comparable to that estimated for other objects analyzed by Wandel et al. (1999).

However, Wandel et al. (1999) would not have obtained the same results as we have because of several different assumptions. First, they assumed that $U n_e = 10^{10}$ uniformly, although it is not clearly explained why this value is used. We use the values inferred from the photoionization analysis for the conditions in the C III]–emitting region: $U = 0.008$ and $n_e = 10^{10.25}$ cm^{-3}. These yield $U n_e = 10^{8.2}$, a number that is much smaller than that assumed by Wandel et al. (1999). The lower value of $U n_e$ that we use increases the inferred mass. Second, we use the velocity width of C III], whereas they use the velocity width of Hβ, which is typically narrower. In IRAS 13224$-$3809 we measured Hβ FWHM of 800 km s^{-1}, although we note that this could be contaminated by Hβ from the starburst, and therefore the width could be underestimated. The larger value of the velocity that we use increases the inferred mass. Recomputing the photoionization mass using $U n_e = 10^{10}$ and $v_{\rm FWHM} = 800$ km s^{-1} gives a photoionization mass of $M_{\rm ph} = 2.4 \times 10^6 M_\odot$. Using their relationship between photoionization and reverberation black hole masses gives $M_{\rm BH} = 4.3 \times 10^6 M_\odot$. This is lower than the estimate based on the assumption that the object is radiating at the Eddington luminosity, implying that it is super-Eddington.

How can we reconcile these differences? A number of factors may influence our mass estimate. As mentioned in § 3.1, the intermediate-ionization line-emitting region may see a lower flux than we do because of $\cos \Theta$ dependence of the emission (Laor & Netzer 1989). It may be that the velocities in the intermediate-ionization line region are higher than the Keplerian velocity due to the gravitational potential presented by the heavy accretion disk (Huré 2002). Both of these factors would decrease the estimate of the black hole mass required by the intermediate-ionization disk lines.

On the other hand, it may be premature to apply the reverberation-mapping results in bulk to all NLS1's. Only a couple of the objects that have been heavily monitored and are considered by Wandel et al. (1999) have optical emission line properties that securely classify them as NLS1's (NGC 4051 and Mrk 335); Mrk 110 is better classified as a low-luminosity Seyfert 1.5. Given the range of UV properties exhibited by NLS1's, as discussed in Paper I, are these too few to draw conclusions about the behavior of the entire class? It is also possible that some of the conclusions obtained from the reverberation-mapping results are compromised

by selection effects. It is well known that the Seyfert-luminosity objects that have been intensively monitored were chosen because their Balmer lines were already known to be variable; the quasars, on the other hand, were chosen without such bias. Kaspi et al. (2000) report that in the reverberation-mapped sample, there is an anticorrelation between luminosity and Balmer emission line velocity width; this is opposite to the expectation of theoretical arguments (e.g., Laor 1998) and to what is observed in other quasar samples.

Finally, we note that this difficulty in reconciling the results of photoionization modeling with the small black hole masses inferred from reverberation mapping (and in apparent agreement with galactic bulge masses as well) may be similar to the apparent difficulty in producing the optical continuum described by Collin & Huré (2001) and Collin et al. (2002).

REFERENCES

Agol, E., Krolik, J., Turner, N. J., & Stone, J. M. 2001, ApJ, 558, 543
Anderson, S. F., et al. 2001, AJ, 122, 503
Arav, N., & Li, Z.-Y. 1994, ApJ, 427, 700
Arav, N., Li, Z.-Y., & Begelman, M. C. 1994, ApJ, 432, 62
Baldwin, J., Ferland, G., Korista, K., & Verner, D. 1995, ApJ, 455, L119
Baldwin, J. A. 1977, ApJ, 214, 679
Baldwin, J. A., et al. 1996, ApJ, 461, 664
Bechtold, J., et al. 2003, ApJ, 588, 119
Blaes, O., & Socrates, A. 2001, ApJ, 553, 987
Boller, Th., Brandt, W. N., Fabian, A. C., & Fink, H. H. 1997, MNRAS, 289, 393
Boroson, T. A., & Green, R. F. 1992, ApJS, 80, 109
Boroson, T. A., & Meyers, K. A. 1992, ApJ, 397, 442
Bottorff, M., Ferland, G., Baldwin, J., & Korista, K. 2000, ApJ, 542, 644
Brotherton, M. S., Wills, B. J., Francis, P. J., & Steidel, C. C. 1994a, ApJ, 430, 495
Brotherton, M. S., Wills, B. J., Steidel, C. C., & Sargent, W. L. W. 1994b, ApJ, 423, 131
Casebeer, D., & Leighly, K. M. 2004, ApJ, submitted
Castor, J. I., Abbott, D. C., & Klein, R. I. 1975, ApJ, 195, 157
Collin, S., Boisson, C., Mouchet, M., Dumont, A.-M., Coupé, S., Porquet, D., & Rokaki, E. 2002, A&A, 388, 771
Collin, S., & Huré, J.-M. 2001, A&A, 372, 50
Constantin, A., Shields, J. C., Hamann, F., & Foltz, C. B. 2002, ApJ, 565, 50
deKool, M., & Begelman, M. C. 1995, ApJ, 455, 448
Dietrich, M., Hamann, F., Shields, J. C., Constantin, A., Vestergaard, M., Chaffee, F., Foltz, C. B., & Junkkarinen, V. T. 2002, ApJ, 581, 912
Fan, X., et al. 1999, ApJ, 526, L57
Ferland, G. J. 2001, HAZY: a Brief Introduction to CLOUDY, ver. 96.00 (Lexington: Univ. Kentucky)
Frank, J., King, A., & Raine, D. 1992, Accretion Power in Astrophysics (Cambridge: Cambridge Univ. Press)
Gallagher, S. C., Brandt, W. N., Chartas, G., & Garmire, G. C. 2002, ApJ, 567, 37
Goodrich, R. W. 1989, ApJ, 342, 224
Hamann, F., & Korista, K. T. 1996, ApJ, 464, 158
Hamann, F., Korista, K. T., Ferland, G. J., Warner, C., & Baldwin, J. 2002, ApJ, 564, 592
Huré, J.-M. 2000, A&A, 358, 378
———. 2002, A&A, 395, L21
Kaspi, S., Smith, P. S., Netzer, H., Maoz, D., Jannuzi, B. T., & Giveon, U. 2000, ApJ, 533, 631
Korista, K., Baldwin, J., Ferland, G., & Verner, D. 1997, ApJS, 108, 401
Korista, K. T., et al. 1995, ApJS, 97, 285
Kramer, R. H., Cohen, D. H., & Owocki, S. P. 2003, ApJ, 592, 532
Krolik, J. H., & Kallman, T. R. 1988, ApJ, 324, 714
Kuraszkiewicz, J., Wilkes, B. J., Czerny, B., & Mathur, S. 2000, ApJ, 542, 692
Laor, A. 1998, ApJ, 505, L83
Laor, A., Fiore, F., Elvis, M., Wilkes, B., & McDowell, J. C. 1997a, ApJ, 477, 93
Laor, A., Jannuzi, B. T., Green, R. F., & Boroson, T. A. 1997b, ApJ, 489, 656
Laor, A., & Netzer, H. 1989, MNRAS, 238, 897
Leighly, K. M. 1999a, ApJS, 125, 297
———. 1999b, ApJS, 125, 317
———. 2001, in ASP Conf. Ser. 224, Probing the Physics of Active Galactic Nuclei by Multiwavelength Monitoring, ed. B. M. Peterson, R. W. Pogge, R. S. Polidan, & R. W. Pogge (ASP: San Francisco), 293

Leighly, K. M., Halpern, J. P., & Jenkins, E. B. 2004, in ASP Conf. Ser. 311, AGN Physics with the Sloan Digital Sky Survey, ed. G. T. Richards & P. B. Hall (ASP: San Francisco), 277
Leighly, K. M., & Moore, J. R. 2004, ApJ, 611, 107 (Paper I)
Leighly, K. M., Mushotzky, R. F., Nandra, K., & Forster, K. 1997, ApJ, 489, L25
Leighly, K. M., Zdziarski, A. A., Kawaguchi, T., & Matsumoto, C. 2002, in Proc. Workshop on X-Ray Spectroscopy of AGNs with Chandra and XMM-Newton, ed. Th. Boller, S. Komossa, S. Kahn, H. Kunieda, & L. Gallo (MPE: Garching), 259
Liu, B. F., Mineshige, S., Meyer, F., Meyer-Hofmeister, E., & Kawaguchi, T. 2002, ApJ, 575, 117
Mathews, W. G., & Ferland, G. J. 1987, ApJ, 323, 456
Mathur, S. 2000, MNRAS, 314, L17
Murray, N., & Chiang, J. 1998, ApJ, 494, 125
Murray, N., Chiang, J., Grossman, S. A., & Voit, G. M. 1995, ApJ, 451, 498
Nicastro, F., Fiore, F., Perola, G. C., & Elvis, M. 1999, ApJ, 512, 184
Osmer, P. S., & Shields, J. C. 1999, in Quasars and Cosmology, ed. G. Ferland & J. Baldwin (San Francisco: PASP), 235
Osterbrock, D. E. 1989, Astrophysics of Gaseous Nebulae and Active Galactic Nuclei (Mill Valley: University Science Books)
Osterbrock, D. E., & Pogge, R. W. 1985, ApJ, 297, 166
Peterson, B. M., Meyers, K. A., Carpriotti, E. R., Foltz, C. B., Wilkes, B. J., & Miller, H. R. 1985, ApJ, 292, 164
Proga, D., Stone, J. M., & Kallman, T. R. 2000, ApJ, 543, 686
Rees, M. J. 1987, MNRAS, 228, P47
Rees, M. J., Netzer, H., & Ferland, G. J. 1989, ApJ, 347, 640
Richards, G. T., Vanden Berk, D. E., Reichard, T. A., Hall, P. B., Schneider, D. P., SubbaRao, M., Thakar, A. R., & York, D. G. 2002, AJ, 124, 1
Ross, R. R., Fabian, A. C., & Mineshige, S. 1992, MNRAS, 258, 189
Sabra, B. M., & Hamann, F. 2001, ApJ, 563, 555
Shang, Z., Wills, B. J., Robinson, E. L., Wills, D., Laor, A., Xie, B., & Yuan, J. 2003, ApJ, 586, 52
Shields, J. C., Ferland, G. J., & Peterson, B. M. 1995, ApJ, 441, 507
Sigut, T. A. A., & Pradhan, A. K. 2003, ApJS, 145, 15
Snedden, S. A., & Gaskell, C. M. 1999, ApJ, 521, L91
Stevens, I. R., & Kallman, T. R. 1990, ApJ, 365, 321
Tarter, C. B., Tucker, W. H., & Salpeter, E. E. 1969, ApJ, 156, 943
Thompson, K. L. 1991, ApJ, 374, 496
Uttley, P., Edelson, R., McHardy, I. M., Peterson, B. M., & Markowitz, A. 2003, ApJ, 584, L53
Wandel, A., Peterson, B. M., & Malkan, M. A. 1999, ApJ, 526, 579
Weymann, R. J., Morris, S. L., Foltz, C. B., & Hewitt, P. C. 1991, ApJ, 373, 23
Wilkes, B. J., Kuraszkiewicz, J., Green, P. J., Mathur, S., & McDowell, J. C. 1999, ApJ, 513, 76
Wilkes, B. J., Tananbaum, H., Worrall, D. M., Avni, Y., Oey, M. S., & Flanagan, J. 1994, ApJS, 92, 53
Wills, B. J., Brotherton, M. S., Fang, D., Steidel, C. C., & Sargen, W. L. W. 1993, ApJ, 415, 563
Wills, B. J., Laor, A., Brotherton, M. S., Wills, D., Wilkes, B. J., Ferland, G. J., & Shang, Z. 1999, ApJ, 515, L53
Wills, B. J., Shang, Z., & Yuan, J. M. 2000, NewA Rev., 44, 511
York, D. G., et al. 2000, AJ, 120, 1579
Young, A. J., Crawford, C. S., Fabian, A. C., Brandt, W. N., & O'Brien, P. T. 1999, MNRAS, 304, L46